DISPERSION BASED PHOTONIC-CRYSTAL STRUCTURES FOR RF APPLICATIONS

Dennis W. Prather, Ph.D.
University of Delaware
Department of Electrical and Computer Engineering
140 Evans Hall, Room 217B
Newark, DE, 19716-3130
Tel: (302) 831-8170, Fax: (302) 831-4316, Email: dprather@ee.udel.edu

ABSTRACT

The development of photonic crystals (PhCs) has enabled groundbreaking approaches to mold the flow of electromagnetic waves with frequency spanning optical regime to RF regime. Periodic electromagnetic materials (RF PhCs) are presently one of the most rapidly advancing sectors in the electromagnetic arena. Herein, we demonstrated the applications of RF PhCs in improving the performance of naval communication system and decreasing scattering cross-section of naval vessels. To this end, we designed, fabricated, and characterized dielectric devices based on the unique dispersion properties of PhCs to achieve confinement, waveguiding, radiation, and filtering in the microwave to millimeter-wave portion of the electromagnetic spectrum. In particular, we experimentally demonstrated dispersion-based guiding in 2D and 3D PhCs. Dispersion-based guiding, namely self-collimation, allows for creating "non-diffractive materials", in which electromagnetic waves can propagate along subwavelength-sized channels without divergence while no specific route is introduced. In addition, by combining the self-collimation PhCs, we demonstrated dielectric grating antennas which provide stable performance, compact dimensions, high radiation efficiency, and high coupling efficiency with other dielectric waveguiding devices. Furthermore, we designed, fabricated, and demonstrated RF channelizers and filters based on the hybrid of properties and lattices of PhCs. Our work provides a framework for establishing dielectric-based naval communication systems, which are more secure and more efficient compared to current metallic counterparts. In this framework, all communication functions, i.e. generating, sending, transmitting, receiving, and processing RF signals, are realized using dielectric devices, which can be embedded within structural composite materials thereby afford low cross-section, RF functionality, and structural support.

1.0 INTRODUCTION

Photonic crystals (PhCs) were proposed as 1D, 2D, or 3D periodic, often dielectric and artificial structures, which are designed to be analogous to semiconductor crystals naturally formed by periodic arrangements of atoms or molecules[1,2]. The propagation of electromagnetic waves in a PhC is governed by Maxwell's equations with the periodic boundary condition defined by the periodic PhC structure, which are analogous to Schrodinger's equations for semiconductor crystals. The solution to the Maxwell's equations results in photonic band-structurelike dispersion relationship between frequency, ω, and wavevector, k. Photonic dispersion relationship governs

the propagation of photons in the photonic crystal, mimicking electronic dispersion relationship in semiconductors. Photonic crystals were experimentally demonstrated for effectively controlling photons in the same way as that semiconductor crystals control electrons, and PhCs are therefore envisioned as the semiconductors for photons. The development of PhCs has enabled groundbreaking approaches to mold the flow of electromagnetic waves with frequency spanning optical regime to RF regime.

First of all, photonic bandgaps (PBGs) can be obtained between neighboring bands if a suitable structure is chosen. For frequencies in a photonic bandgap, the propagation of light is completely prohibited regardless of any propagation direction[3,4,5]. In this sense, PhCs with photonic bandgaps, namely PBG materials, are optical insulators. However, if a point defect is introduced, a high-Q cavity for efficient light confinement and emission can be formed[6,7,8]. Design of cavities responding to different frequencies can give rise to high-performance channel-drop filters[9,10]. Similarly, if a line defect[11,12] or a series of coupled-cavities[13,14,15,16] are incorporated into such a PhC, light propagation can be completely confined along a specific path[17,18,19]. In addition to nanocavities and waveguides, PBG materials have enabled the creation of compact optical switches[20,21] and micrometer-sized lasers[22]. Photonic bandgap materials also found applications in enhancing efficiency of light emission[23] and microwave antenna[24]. "Bandgap plus defects" is a good formula for solving the problem of photon localization and light beam routing.

Furthermore, PhCs as a new category of materials provide novel optical properties that cannot be achieved in regular materials. In particular, closer study of full-wavevector dispersion diagrams for different PhCs has revealed unique dispersion properties, by which some first-ever effects have been realized. Unique dispersion-related phenomena include negative refraction[25,26], superprism[27,28], self-collimation[29,30], and slowing light[31]. The applications of these dispersion properties in optical regime have enabled new approaches for developing high performance photonic integrated devices. On the other hand, by dimensional scaling, the applications in optical regime can find their corresponding applications in RF regime, which may give rise to revolutionary improvement in the performance of RF devices. Photonic crystals allow us to engineer control over the propagation of electromagnetic waves to an extent that was previously not possible. As a result, periodic electromagnetic materials (RF PhCs) are presently one of the most rapidly advancing sectors in the electromagnetic arena. Owing to the tremendous potential of RF PhC structures, there is a plethora of applications in which these can be used.

We proposed to apply RF PhCs in improving the performance of naval communication system and decreasing scattering cross-section of naval vessels. A dominant aspect in the design of most naval platforms is the incorporation of functional RF devices and systems, including waveguides, routing networks, and antennas. Unfortunately, in many cases this comes at the expense of reducing structural support and increasing scattering cross-sections. One means to address this is to design ship superstructures using advanced composite materials that consist of mainly *dielectric* materials. In this case, their RF scattering properties are far less than their all metallic counterparts. However, once the superstructure and masts are in place, albeit with low RF cross-sections, they are typically outfitted with communication and radar antennas that serve to compromise their structural integrity. In addition, there is often a significant increase in scattering cross-section due to the introduction of metallic waveguides that serve to feed and receive antennas that are also mounted on the superstructure. To overcome this limitation, we need to develop novel routing and radiation structures that are largely electromagnetically transparent yet based on their unique dispersion properties still guide and radiate electromagnetic waves.

In addition to reducing the scattering properties of waveguides and antennas in ship superstructure, there is also a rising problem with the limitation by space and location considerations due to the numerous radiating apertures that are needed. Moreover, antennas are typically placed on shipboard locations that profoundly affect their radiation patterns in comparison to their initial designs. As a result, antenna performance can be significantly altered as can the RF signature of the ship, due to the significant scattering effects of having a large metallic object located high above deck. To overcome these limitations, we propose the design and fabrication of dispersion-based antennas that can be directly molded into the dielectric composite materials, which comprise the ship's superstructure.

In this effort, we designed, fabricated, and demonstrated routing and radiating structures in the microwave to millimeter-wave portion of the electromagnetic spectrum. These devices are based on the unique dispersion properties of photonic crystals to achieve confinement, waveguiding, radiation, and filtering. The main advantage of this approach over conventional techniques is that dispersion elements are to a large extent electromagnetically transparent and therefore have significantly reduced scattering cross-sections. In addition, such structures can be embedded directly into composite material structures to thereby maintain structural integrity.

2.0 TECHNICAL ACCOMPLISHMENTS

To this end, we focused our work in experimental demonstration of *dispersion-based guiding* in 2D and 3D photonic crystals and *dielectric grating antenna systems*. Dispersion-based guiding, namely self-collimation, allows for creating "non-diffractive materials", in which electromagnetic waves can propagate along subwavelength-sized channels without divergence while no specific route is introduced. The applications of this novel effect include high-density waveguiding with low channel crosstalk and high coupling efficiency with other dielectric devices. Dielectric grating antennas provide stable performance, compact dimensions, high radiation efficiency, and high coupling efficiency with other dielectric waveguiding devices. In addition, all materials used in our devices are dielectric, which can be embedded within structural composite materials thereby afford low cross-section, RF functionality, and structural support.

The research was carried out in five steps. The first step consisted of the development of a millimeter-wave imaging system for mapping the field distribution (amplitude and phase) in a 3D volume. Although the fabrication of millimeter-wave PhCs may be less challenging than that of near infrared (NIR) or visible light, the corresponding detection system for millimeter-wave is much more complex than an NIR or visible camera. In millimeter-wave regime, the amplitude and phase of a coherent wave at a given point can be measured using a monopole connected to a vector network analyzer. As a result, the detection system for mapping the field distribution in a 3D volume was established by 3-dimensionally scanning the monopole. A particularly attractive feature of this system is its ability to measure results in both amplitude and phase.

The second step was to design, fabricate, and demonstrate self-collimation guiding in low index contrast photonic crystals. The design of the PhCs is based on their equi-frequency contours and the 2D finite-difference time-domain simulation results. In the experiments, the millimeter-wave photonic crystals are fabricated in Rexolite slabs by a computer numerically controlled (CNC) micro-milling system. Using the millimeter-wave imaging system, we have observed and characterized the self-collimation (dispersion guiding) effect for both the amplitude and phase of the propagating electromagnetic wave in low index contrast photonic crystals.

As the third step, we designed, fabricated, and characterized a millimeter-wave grating antenna with an integrated self-collimation photonic crystal. The photonic crystal provides a

collimated beam feed to the grating antenna by reshaping the wave front using its unique dispersion properties. The parameters of the photonic crystal and that of the grating are chosen so that self-collimation for the photonic crystal and normal scattering for the grating occur simultaneously at 40GHz. This integration constitutes a potential improvement on the overall performance of the antenna. Experimental results showed good directivity and high radiation efficiency.

As the fourth step, we investigated and experimentally demonstrated self-collimation guiding inside a 3D simple cubic PhC at microwave frequencies. If the significance of demonstration of self-collimation in 2D planar structures lies in providing a novel guiding approach, then the significance of demonstration of 3D self-collimation lies in opening the door to a completely new category of materials, namely "non-diffractive materials". The self-collimation modes were excited by a grounded waveguide feeding and detected by a scanning monopole. Self-collimation of electromagnetic waves in the 3D photonic crystal was demonstrated by measuring the 3D field distribution, which was shown as a narrow collimated beam inside the 3D photonic crystal, but a diverged beam in the absence of the photonic crystal.

Furthermore, if sensors and communication devices, such as channelizers and correlators, are incorporated into these superstructures, it will provide capabilities of direct capturing, digitalizing, and analyzing electromagnetic signals at the receiving end. Meanwhile, it can greatly increase the structural support and compactness. To this end, we designed, fabricated, and demonstrated RF channelizers and filters based on the hybrid of properties and lattices of photonic crystals. Most part of research in this aspect will be carried out in PHASE II.

The work accomplished in PHASE I combining that will be finished in PHASE II will provide a totally new outlook for dielectric-based RF communication systems (e.g., naval platforms), where all communication functions, i.e. generating, sending, transmitting, receiving, and processing RF signals, are realized using dielectric devices.

2.1 SELF-COLLIMATION GUIDING IN A 2D PHOTONIC CRYSTAL

Electromagnetic beams diverge when propagating in dielectric materials due to diffraction. It seems to be a universal rule that no material can sustain and preserve the size of a narrow beam unless specific structural routes (e.g. waveguides, index gradients[32], or line-defects[13]) are incorporated. Recently, development of PhCs[1,2] has enabled groundbreaking approaches to control the flow of electromagnetic waves. Many applications of PhCs stem from the existence of a photonic bandgap in a certain frequency range, where no electromagnetic wave is permitted to propagate. If defects are introduced in PBG materials, localized modes can be excited. The localized modes can be either cavity modes for point defects[33,34] or guiding modes for linear defects[35]. In this sense, PBG provides a powerful guiding approach since the guiding route, which depends on the defects incorporated in the PhC, can be extremely narrow and sharply bent[33]. However, this guiding mechanism, namely "bandgap plus defects," also has drawbacks. For instance, photonic bandgap requires high index contrast, which limits the material selection and often results in large index mismatch at interfacial boundaries. On the other hand, recently substantial interest has arisen in the unique dispersion properties provided by PhCs[36, 37, 38]. A particular phenomenon for PhCs is self-collimation[29,30]. When a PhC works in self-collimation mode, an electromagnetic beam can propagate within it without divergence. In other words, electromagnetic wave propagates as if there were no diffraction in the material.

The concept of self-collimation was originally proposed by Kosaka, et al [29], followed by a detailed theoretical investigation by Witzens, et al [30] and Chigrin, et al[39]. Chen, et al [40] and Yu, et al [41] theoretically discussed the bending, crossing, and splitting properties for self-collimation PhCs. However, most of their effort was focused on high index contrast PhCs[42,43]. To decrease the coupling loss between common materials and a PhC, we focus our work on low refractive index contrast PhCs[44]. In our work, we designed, fabricated PhCs and experimentally demonstrated, for the first time, self-collimation effect using both amplitude and phase, for low index contrast PhCs.

The dimensions for all PhCs are scalable with regard to the working wavelength because there is no fundamental constant with the dimensions of length in Maxwell's equations[45]. As a result, the feature size for near infrared (NIR) or visible light is on the order of 100's nanometers, while that for millimeter-wave (MMW) is on the order of 100's microns. Therefore, the fabrication of MMW PhCs is less challenging than that of NIR or visible light. However, the corresponding detection system for MMWs is much more complex than an NIR or visible camera. Nevertheless, we have built a MMW imaging setup, as shown in Fig. 1, based on an Agilent 85106D network analyzer, which encompasses a test and measurement capability spanning 45MHz through 110GHz.

A particularly attractive feature of this system is its ability to measure results in both amplitude and phase. To this end, the setup is composed of 3 subsystems: MMW feed system, motion control system, and S-parameter measurement system. In our setup, the sample is placed on the top, while the input source, from port 1, is launched either through a monopole antenna (source 1) or a waveguide (source 2), which works as a point source or windowed beam, respectively. To avoid the potential of distributing the fields during measurement, the detector chosen is simply a 1mm monopole antenna, which is fed back into port 2 of the network analyzer. The field distribution is acquired by scanning the surface of the PhCs to detect the evanescent waves of the MMW propagating in the slab. To do this, we assumed the gap between the detector and the surface is constant, in which case the evanescent wave distribution is proportional to the field in the PhCs. A custom program was developed to synchronize the scanning and measurement. Once a scanning and measurement is finished, we depict the S-parameter value

with regard to the position as an image. Consequently, each pixel in the image corresponds to the S-parameter (S_{21} in our case) value at a scanning position. Also, in the network analyzer the S-parameters are given as complex values, so we can obtain both amplitude and phase distributions, which is impractical for NIR or visible light measurement.
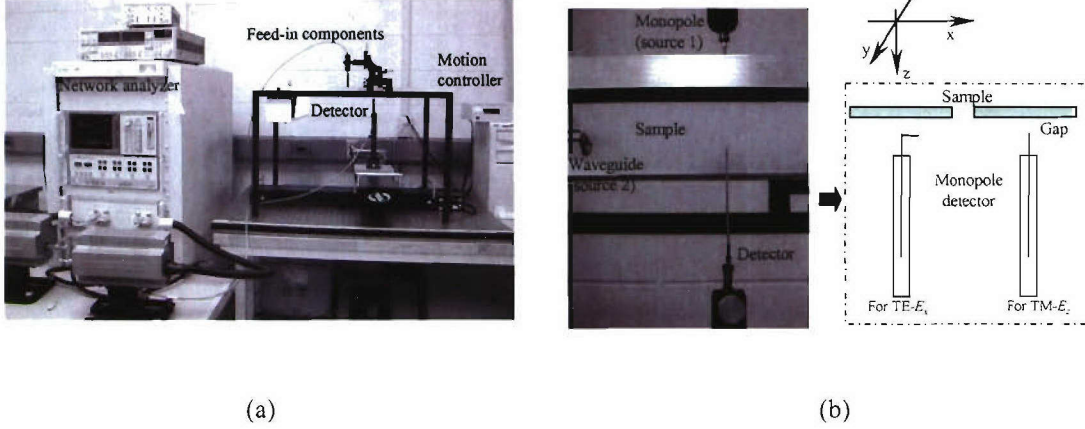

(a)   (b)

Fig. 1. The MMW imaging setup based on a network analyzer: (a) The whole system; (b) The MMW feeds and the detector.

In order to demonstrate self-collimation, a MMW material, 2.4mm (or 3/32-inch) thick Rexolite® slab, is used in our work. Rexolite, a plastic-like material with index of 1.58, has the advantage of easy fabrication, low loss, and low cost. In particular, it can be fabricated using a CNC micro-milling machine. Also, its low index provides a weaker confinement in the slab for MMW on vertical direction, resulting in a stronger evanescent wave for detection. In order to determine the dielectric constant or index, we first launched of the Rexolite slab a 40GHz MMW and scanned the Rexolite slab (thickness: 2.4mm) without any pattern. We then calculated the effective index of the slab according to the guided wavelength, which can be easily calculated from the measured phase distribution. The effective index, defined as

$$n_{eff} = n \sin\theta_{mode}, \tag{1}$$

can be calculated as

$$n_{eff} = \beta_z/\beta_0 = \lambda_0/\lambda_g, \tag{2}$$

where λ_0 is the vacuum wavelength and λ_g is the guiding wavelength along the slab.

The measured values are n_{eff}(TE) =1.36, and n_{eff}(TM)=1.21, which are very close to the calculated values, n_{eff}(TE) =1.36 and n_{eff}(TM)=1.23 based on the ray-tracing method [46]. Applying these effective indices, we calculated the EFCs for a square lattice PhC with the hole diameter to lattice constant ratio $2r/a$=0.6 using a plane-wave expansion method [47]. In Fig. 2, the results of this calculation are shown as the normalized frequency

$$\omega_n = \omega a/2\pi c \tag{3}$$

and the normalized wavevector

$$k_n = ka/2\pi, \qquad\qquad (4)$$

where c is the speed of light.

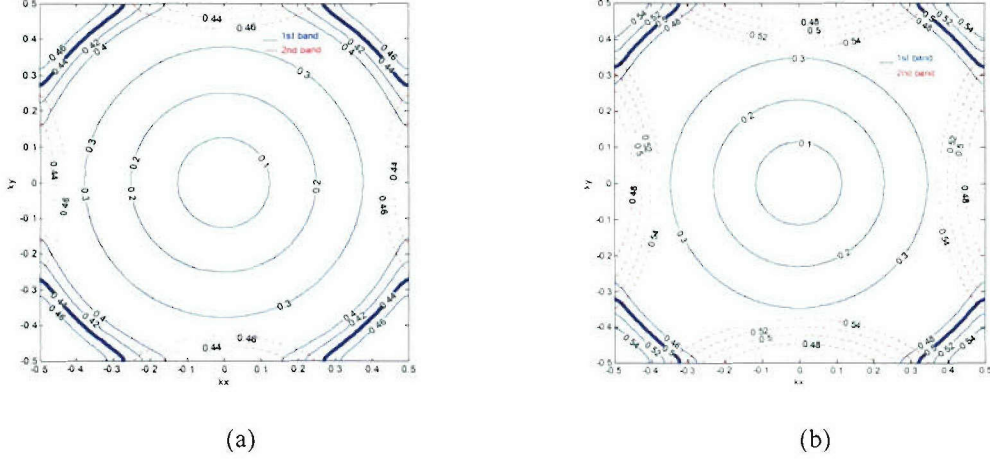
(a)   (b)

Fig. 2: Equi-frequency dispersion contours for 2.4mm thick Rexolite square lattice PhC(2r/a=0.6): (a) for TE mode(n_{eff}=1.36); (b) for TM mode(n_{eff}=1.21).

By observing the EFCs, we anticipate that self-collimation in the first band will occur at normalized frequencies of ω_n=0.44 for TE, and ω_n=0.50 for TM because at these frequencies the EFCs are nearly flat and the excited mode will propagate with group velocities pointing at almost the same direction (45° to the lattice orientation), which is calculated from[48]

$$v_g = \nabla_k \omega(k) . \qquad\qquad (5)$$

In the 2nd band, frequencies shown in Fig. 2 cannot excite self-collimated mode, but self-collimation can really occur at higher frequencies. However, parts of their EFCs are located inside of the so-called "light cone" and results in a large propagation loss [49]. Light cone represents that on vertical direction of the slab the total internal reflection is *just* satisfied at that frequency, or $k_n=\omega_n$. Consequently, light cannot be fully confined at vertical direction of the slab due to violation of the total internal reflection condition. In a contrast, in our work we chose the 1st band because the EFCs of the MMW with these frequencies lie outside their light cones, and hence energy can propagate with minimum loss.

In order to examine the self-collimation effect at around 40.0GHz, we selected the following parameters: hole diameter $2r$=2.00mm and lattice constant $a=2r/0.6$=3.33mm. In our case, two-dimensional PhCs are fabricated by drilling regularly aligned holes through the Rexolite slabs. In the zooming-in inset of Fig. 3 (a), the holes are illustrated in white. The nearest neighboring distance between holes is lattice constant a. Since the first band at the selected frequency is at an angle of 45° to the lattice orientation, for observational convenience, we rotate the PhC lattice orientation at 45° with respect to the waveguide feed, as shown in Fig. 3 (a). Although the self-collimation should be optimal at ω_n=0.44, we examine the frequency ω_n=0.42 to avoid the degeneracy with the second band because, as shown in Fig. 2 (a), eignvalues only exist at the 1st band (solid lines) for ω_n=0.42, while eignvalues exist both at the 1st band and the 2nd band (dashed lines) for ω_n=0.44.

Point source
feed here

Waveguide feed here

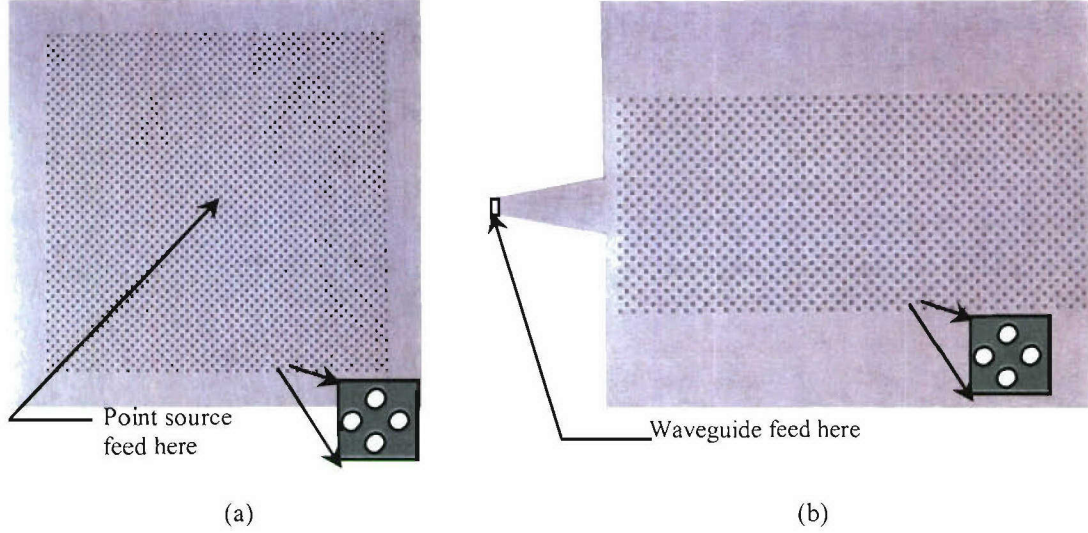(a)   (b)

Fig. 3: MMW Rexolite PhCs fabricated by the micro-milling method: (a) PhC for TE self-collimation;
(b) PhC for TM self-collimation. Both of them are with hole diameter 2r=2.00mm and lattice constant
a=2r/0.6=3.33mm. The horn has the dimensions of w6×L40×W18mm.

According to the normalized frequency, we can calculate the vacuum wavelength, $\lambda_0 = a/\omega_n$ = 7.8 mm, and the corresponding frequency is about 39GHz. Based on the 2D finite-difference time-domain (FDTD) method[50], we simulated a 39.0 GHz TE MMW from a monopole source propagating in the PhC, as shown in Fig. 4 (a). For TE modes, the MMWs have three dominant components, E_x, E_y, and H_z. Either the distribution of magnetic field, H_z, or electrical field, $E = \sqrt{E_x^2 + E_y^2}$, indicates directions of the power distribution. It is easier to measure the electrical field, so we show the amplitude of the electrical field in the simulation. Thus, the simulation shows the propagation is primarily in two orthogonal directions, which indicates the presence of self-collimation. In contrast, it is well known that the propagation is isotropic among common materials.

For TM modes, the effective index is much smaller. As a result, self-collimation only occurs over a very narrow incident angle range and the degeneracy with the second band is inevitable because, as shown in Fig. 2 (b), eignvalues exist both at the first band (solid lines) and the 2nd band (dashed lines) for frequencies spanning from 0.48 to 0.54, whose EFCs are acceptably straight. We chose ω_n=0.5, which corresponding to MMW with vacuum wavelength, $\lambda_0 = a/\omega_n$ = 6.67mm, and frequency 45GHz for the PhC with a=2r/0.6=3.33mm, and launched a windowed beam (with the dimension of WR-22 waveguide, w=5.6mm) instead of a monopole as the input, as shown in Fig. 3 (b). Also, the input is expanded through an integrated horn with dimensions $w6×L40×W18$mm, by which the launched MMW is expanded to an 18mm windowed beam at the distance of 40mm. Applying the 2D FDTD method, we show that, in Fig. 4 (b), the 45GHz TM MMW is self-collimated even for this PhC with such a low index contrast. For TM modes, the MMW has only one electric component, i.e., $E=E_z$.
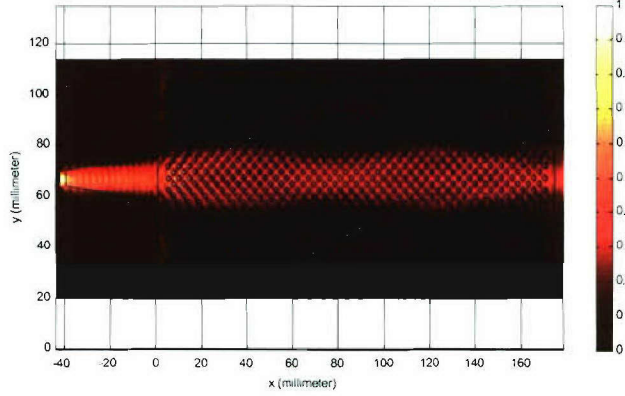
Fig. 5 shows the experimental results. From the images we can see that the E_x distribution is along y-axis, while the E_y distribution is along x-axis. The relative amplitude of E_z is calculated from

8

$$E \propto \sqrt{E_x^2 + E_y^2} \; . \tag{6}$$

The image of E shows that the propagation is primarily along two directions, namely x-axis and y-axis, and as a result the MMW is self-collimated.
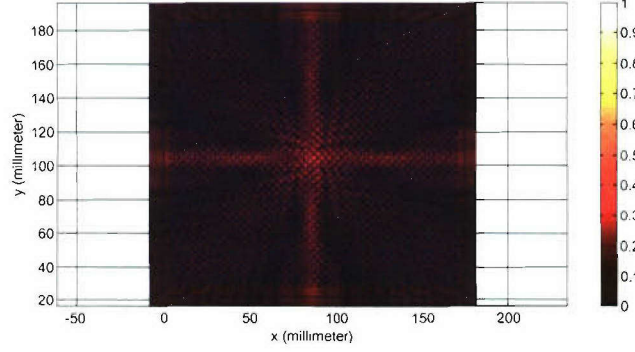
(a)

(b)

Fig. 4: (a) Simulation of amplitude H_z when a 39GHz TE monopole MMW propagates in the designed PhC; (b) Simulation of amplitude E_z when a 45GHz TM MMW fed from a horn propagates in the designed PhC. Both PhCs with hole diameter $2r=2.00mm$ and lattice constant $a=2r/0.6=3.33mm$.

To verify these results experimentally, we first fabricated $(69 \times 69 + 1)/2$ holes according to the simulated structure in a Rexolite slab and cleaved it into a 200mm×200mm square with holes aligned in the middle of the slab as shown in Fig. 3 (a). Since for TE modes the electric filed component is polarized in the slab, we bent the source monopole as well as detection monopole 90° to ensure they were parallel to the slab as illustrated in Fig. 1(b). We inserted the source monopole in the center hole, set the frequency at 39GHz, and scanned the slab with steps $dx=dy=0.5mm$. To measure E_x, the detecting monopole antenna was placed along x-axis, and E_y, y-axis.

To experimentally validate TM self-collimation, we first fabricated the PhC structure with $(33 \times 71 + 1)/2$ holes and then cleaved it into a slab with the designed fed-in horn, as shown in Fig. 3 (b). In our experiment, we fed this PhC with a WR-22 waveguide with dimensions 5.6mm×2.8mm. In this case, the waveguide excites TE_{01} mode and electrical field (or E-vector) is polarized along the narrower side of the waveguide. We rotated the waveguide, making sure that

the E-vector was perpendicular to the slab. The detecting monopole antenna was straight, coinciding with the E-vector as illustrated in Fig. 1 (b). We set the frequency at 45GHz and scanned the slab with steps $dx=dy=0.5$mm.
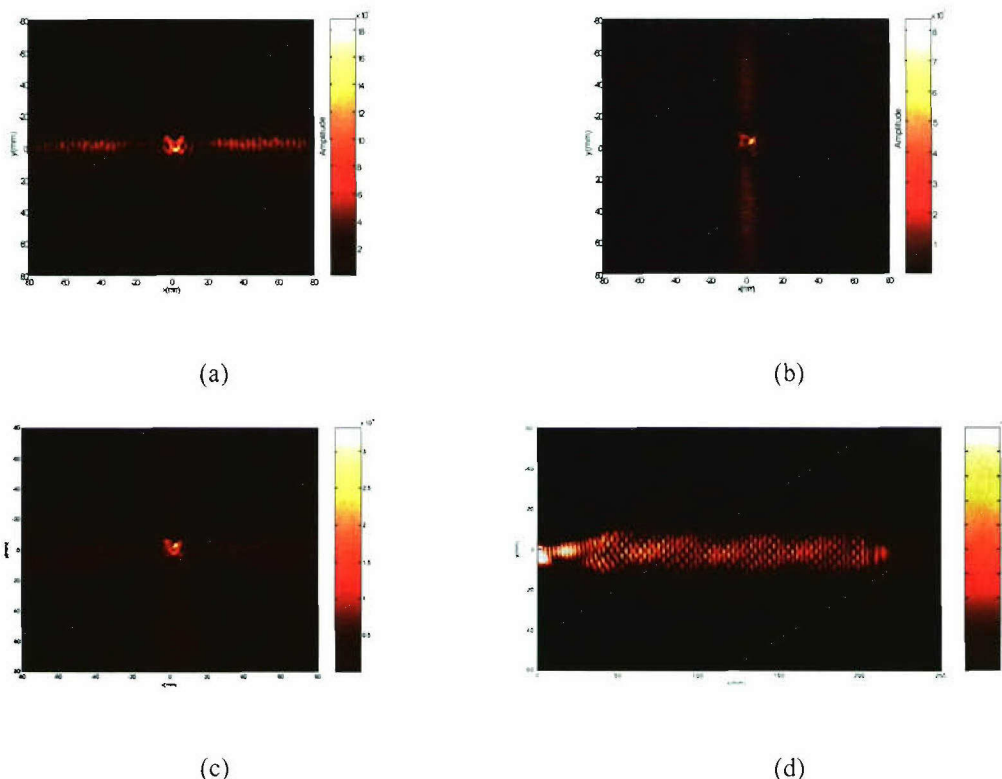

(a)

(b)

(c)

(d)

Fig. 5: Images of a 39GHz TE monopole MMW propagating in the fabricated PhC: (a) Image of E_y; (b) Image of E_x; (c) Image of H_z calculated from images of E_y and E_x, $H_z \propto \sqrt{E_x^2 + E_y^2}$; (d) Image of E_y for 39GHz TE MMW propagating in the fabricated PhC. MMW is fed from a waveguide through the integrated horn.

Fig. 6 (a, b) shows the experimental results for amplitude and phase. Images of E_z, both in amplitude and phase, show that the propagation is along only one direction and the MMW is indeed self-collimated even for an effective index as low as 1.21. Also, due to the low contrast the back-reflection at the interface to the PhC is very small. The beats shown in the amplitude might be attributed to deviations from straight lines in the EFC at ends and activity of higher harmonic modes. In addition, by picking up the narrow central rows, we can estimate the propagation loss, which was determined to be 0.1dB/cm.

In contrast, we fabricated another device with the same horn and dimensions, but without the PhC on it. We repeated the experiment and obtained the images for the amplitude and phase, as shown in Fig. 6 (c, d). It is clear that the propagation in this device is not collimated, which serves to prove that the collimation in our PhC device is not originated from the horn.

Based on the same PhC with horn device, we altered the source to 39GHz TE MMW and repeated the experiment. The result is shown in Fig. 5(d). The self-collimation effect for TE mode is validated again. Using the same process as for TM mode, we estimated the propagation loss, which was determined to be 0.2dB/cm. The difference between the loss for TE mode and that for TM mode may be attributed to the different feed beam widths: TM with the width $W_a=5.6$mm and

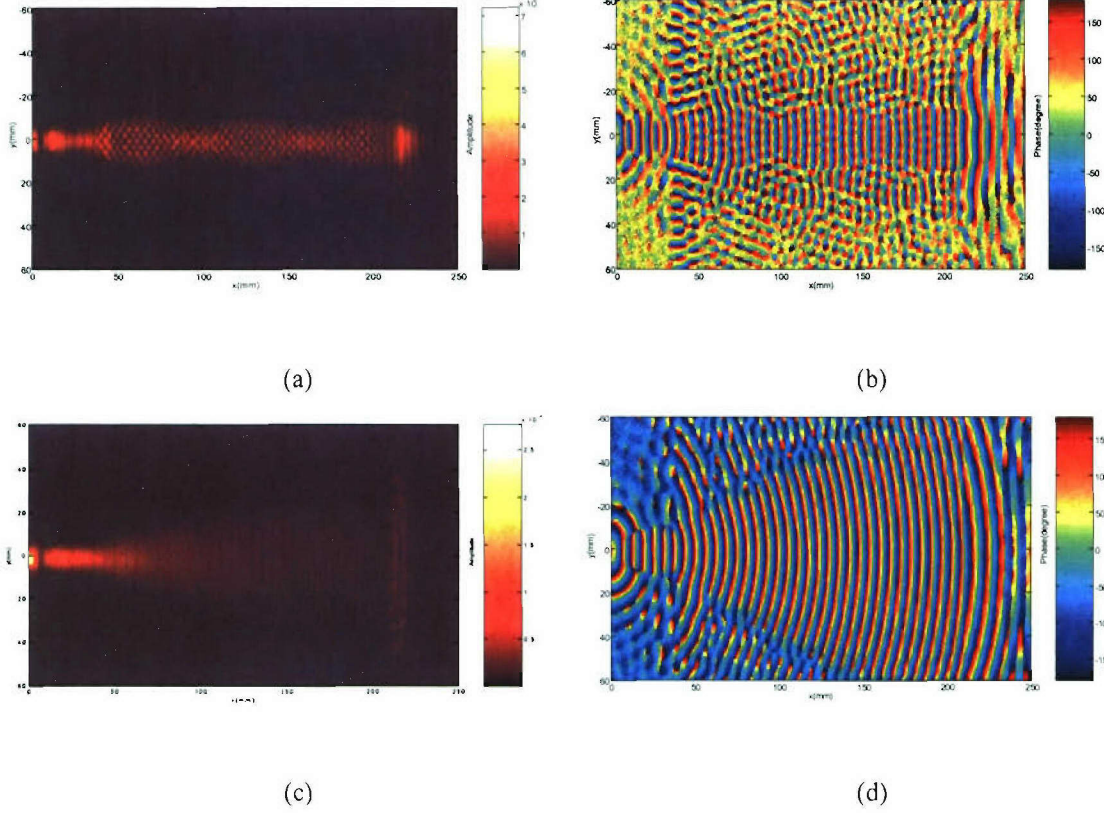TE with the width W_b=2.8mm.

(a)

(b)

(c)

(d)

Fig. 6: (a)(b) Images of E_z (amplitude and phase) for 45GHz TM MMW propagating in the fabricated PhC. MMW is fed from a waveguide through the integrated horn; (c)(d) Images of E_z (amplitude and phase) for 45GHz TM MMW propagating in a device with the same dimensions but without the PhC. MMW is fed from a waveguide through the horn.

We noticed that self-collimation only occurs at some spectral ranges. So we repeated the experiment using the same PhC, but spanned the frequencies from 35GHz to 41GHz for TE, and from 42GHz to 48GHz for TM. We obtained two series of images showing how self-collimation begins and how self-collimation ends with relation to the frequencies. From these images, we conclude that self-collimation is acceptable in the ranges of (38.6GHz, 41.0GHz) for TE mode, and (43.8GHz, 46.2GHz) for TM mode.

2.2 MILLIMETER-WAVE DIELECTRIC GRATING ANTENNA WITH INTEGRATION OF A SELF-COLLIMATION PHOTONIC CRYSTAL

Integrated planar gratings have been widely used in integrated optics as distributed-feedback lasers, mode size converting couplers, and add-drop multiplexers[51,52,53,54]. Recently, considerable interest has risen in the use of all-dielectric grating antennas due to their low loss, low cost, and easy integration with other planar devices[55,56,57]. In particular, grating antennas for millimeter-wave applications can be comparatively compact and provide acceptable directivity. In addition, they offer the capability of beam scanning and steering by varying the grating parameters, or the frequency[58,59]. However, planewave-like feedings are often required when grating antennas are built in; otherwise, their performance will degrade. Recently, we proposed and demonstrated self-collimation photonic crystals (PhCs), which can reshape the wave front into plane waves[60,61,62,63]. Herein, we apply this new technique and demonstrate a millimeter-wave grating antenna with the integration of a self-collimation photonic crystal.
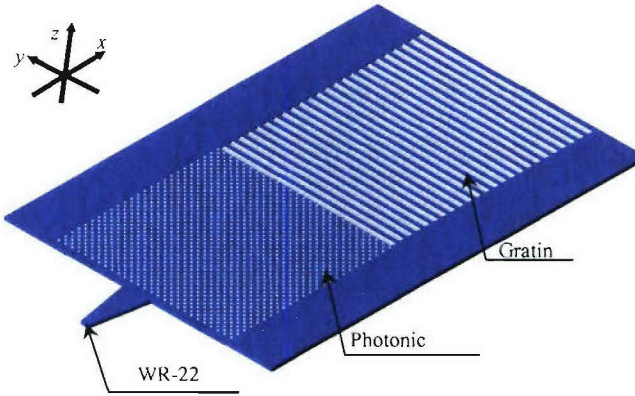
Fig. 7: The schematic of the antenna. The device is composed of a square lattice PhC and a grating structure. The parameters of the PhC (2r=2.0mm, 2r/a=0.6) and the grating (Λ=5.8mm, Δ=2.9mm, Depth=0.6mm) are chosen so that self-collimation for the PhC and normal scattering for the grating occur simultaneously at 40GHz. The thickness of the Rexolite slab is 2.4mm.

Self-collimation occurs when the equi-frequency contours (EFCs) are square-like in shape. When a PhC works in self-collimation modes, an electromagnetic beam propagating within it will do so without divergence. In other words, an electromagnetic wave, or light, is channelized as if it were contained within a linear defect, but no defect is present. Furthermore, the size of the beam depends on that of the feed size and can be large, but the wave front of a self-collimation beam maintains a flat profile regardless of the beam width. This property provides a very good approximation of a plane wave and, hence, a good feed for a grating antenna. In contrast, a standard dielectric waveguide cannot provide a wide and a flat-phase-profile feed due to multiple modes.

Fig. 7 illustrates our proposed device, which is composed of a square lattice PhC and a grating structure. The parameters of the PhC and the grating are chosen so that self-collimation for the PhC and normal scattering for the grating occur simultaneously for a given working frequency. In the description, we use a Cartesian coordination system: the x-axis is along the guiding direction, y-axis is in the device surface, and z-axis is perpendicular to the device surface, see the inset of Fig. 7.
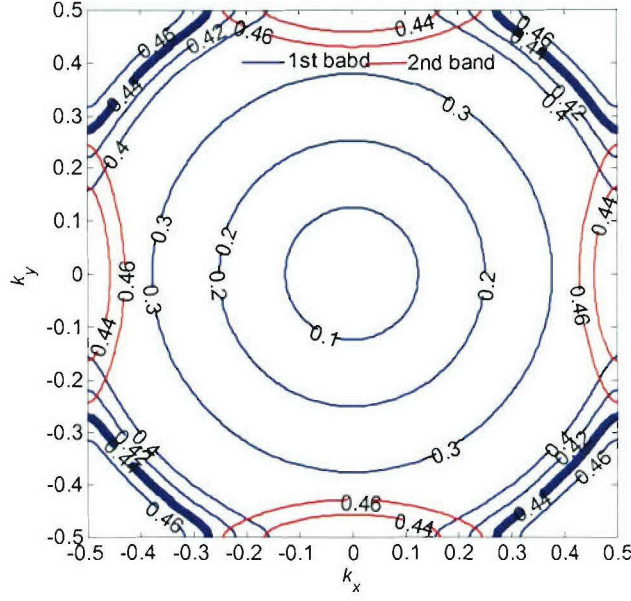
Fig. 8: The equi-frequency contour for the photonic crystal.

The photonic crystal used in this work is similar to that reported in last section. In this work, we used a Rexolite slab with a thickness of 2.4mm and a bulk refractive index of 1.58. To study this planar structure, we employed the effective index method, which simplifies an otherwise 3D problem to a 2D problem with an adjusted index, namely the effective index of the slab. A good approximation for the effective index is $n_{eff} \approx \beta/k_0$, where β and k_0 ($=\omega/c=2\pi/\lambda$) are the propagation constants in the slab and in vacuum, respectively. Since the propagation constants for TE and TM modes are different, the effective indices for TE and TM modes are also different, even with electromagnetic waves of the same frequency propagating in the same slab. For instance, the effective indices for the Rexolite slab are calculated to be n_{eff}(TE) =1.36, and n_{eff}(TM)=1.21 for a propagating wave at 40GHz. As a result, the dispersion properties of a photonic crystal for TE and TM modes will also be different. In this work, we only demonstrate the TE case, where the magnetic field is along z-axis. Applying the effective index method, we calculated the equi-frequency contours of the dispersion surfaces for $2r/a$=0.6 square lattice PhC using the plane-wave expansion method, where a is the lattice constant of the crystalline structure, and $2r$ is the diameter of the circular holes.

In Fig. 8, the results of the calculation are shown for the normalized frequency $\omega_n = fa/c$ and the normalized wavevector $k_n = ka/2\pi$. In the equi-frequency dispersion contours, we anticipate that self-collimation in the first band will occur at a normalized frequency of ω_n=0.44 for the TE mode because at this frequency the equi-frequency contour is nearly straight. In order to design the device to work at 40 GHz, we choose the lattice constant, a=0.44c/f=3.3 mm and the diameter of the hole, $2r$=0.6a=2.0 mm.

The design of the grating structure is based on the phase matching between the scattering wave and guiding wave, which is given from the grating equation[64]:

$$\gamma_x - \beta = \frac{2\pi}{\Lambda} m,$$ (7)

13

where γ_x is the *x*-component of the scattering wave vector, $\beta \ (= n_{eff}\frac{2\pi}{\lambda})$ is the propagation constant, and *m* is an integer. See Fig. 9(a). To achieve normal scattering, γ_x=0. Thus, one straightforward choice is that *m*=-1, resulting $\Lambda = \lambda/n_{eff}$=5.6mm for a TE mode in our slab operating at *f*=40GHz. Appling this grating period in a 2D finite-difference time-domain (FDTD) simulation and carefully tuning the parameters, we verified and optimized the design by evaluating the effect of the grating on n_{eff}. In particular, the grating period should be tuned up because the effective thickness of the slab decreases and, hence, the effective index decreases when the grating pattern is imposed on a blank slab. The simulation results are shown in Fig. 9(b). Accordingly, we selected another structure with the following excitation parameters: slab thickness *T*=2.4 mm, grating period Λ=5.8 mm, grating period aspect ratio Δ/Λ=0.5, grating depth *d*=0.6 mm, source wavelength λ=7.5 mm (*f*=40 GHz), and a source polarization of TE mode.

(a)

(b)
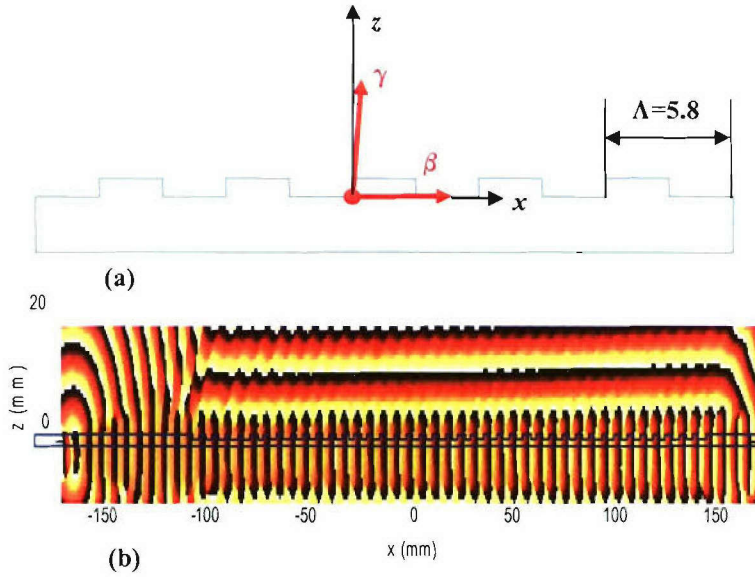
Fig. 9: (a) The illustration showing the principle of the antenna grating. (b) The phase distribution by the two-dimensional FDTD simulation.

In our experiment, we fabricated the device using a computer numerically controlled (CNC) router. A tapered planar structure is incorporated to efficiently feed a launched millimeter-wave into the device. We employed our millimeter-wave imaging system[61,65,66,67] as shown in Fig. 10 to map the near field distribution three-dimensionally. This system is mainly composed of an Agilent 85106D vector network analyzer and an XYZ scanner. In our setup, the sample is placed on the platform, while the input source, from port 1, is launched through a WR-22 waveguide. To avoid the potential of distributing the fields during measurement, the detector chosen is simply a 1mm monopole antenna, which is fed back into port 2 of the network analyzer. The field distribution is acquired by scanning along the surface of the PhCs to detect the propagation and evanescent waves of the MMW propagating in the slab. A custom program was developed to synchronize the scanning with field measurement. Once the scanning and measurement is finished, we depict the S-parameter value, S_{21} in our case, with regard to the position as an image. Consequently, each pixel in the image corresponds to the S-parameter value at each scanning position.
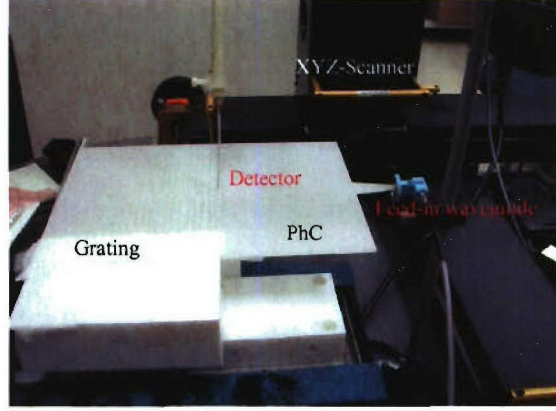
Fig. 10: Experimental setup for charactering the device.

To visualize the field better, we kept the value of the y-axis constant and made a scan along the vertical (x, z) plane. Fig. 11 shows the measured amplitude and phase distributions. From the phase distribution, we can see that the scattering waves are along the z-axis, which is the normal of the device surface and in good agreement with the simulation results shown in Fig. 9 (b). However, the amplitude distribution shown is not yet uniform. This issue may be resolved by carefully chirping the aspect ratio of the grating. Such chirped gratings are still under development and will be reported in future publications.
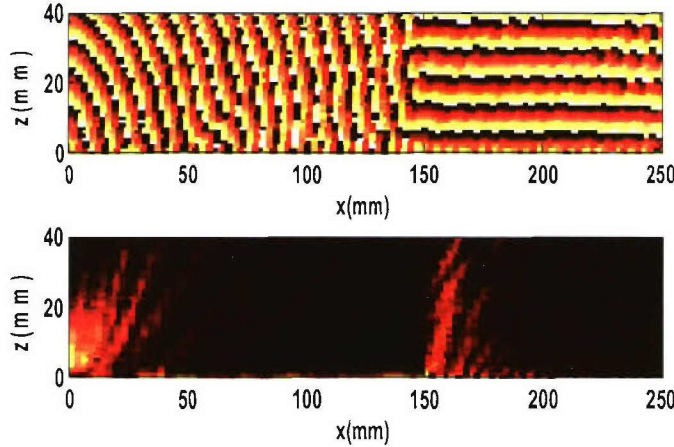
Fig. 11: Field distribution (phase and amplitude) along (xz) plane.

In addition, we also kept value of the z-axis a constant (where the distance to the surface is constant) and made several scans along the horizontal (x, y) plane. Fig. 12(a) shows the amplitude and phase distribution along the horizontal (x, y) plane, when the detector is 7 mm over the device surface. Since the distance is quite large compared with the wavelength, most of the waves sensed by the detector are scattered waves, which propagate into far field. This emission of power makes the grating an antenna (The slight phase variation along x-axis may be attributed to fabrication errors in the grating structure.) On the other hand, Fig. 12(b) shows the amplitude and phase distribution along the horizontal (x, y) plane when the detector is 2mm over the device surface. Since the distance is small compared with the wavelength, most of the waves sensed by the detector are evanescent waves, which exist in the device and propagate as guided waves. The

15

phase distribution shown in Fig. 12(b) is a series of parallel lines. This is attributed to the realization of the self-collimation photonic crystal. The amplitude distribution shown in Fig. 12(a, b) decays because the wave is leaking/scattering through the grating.
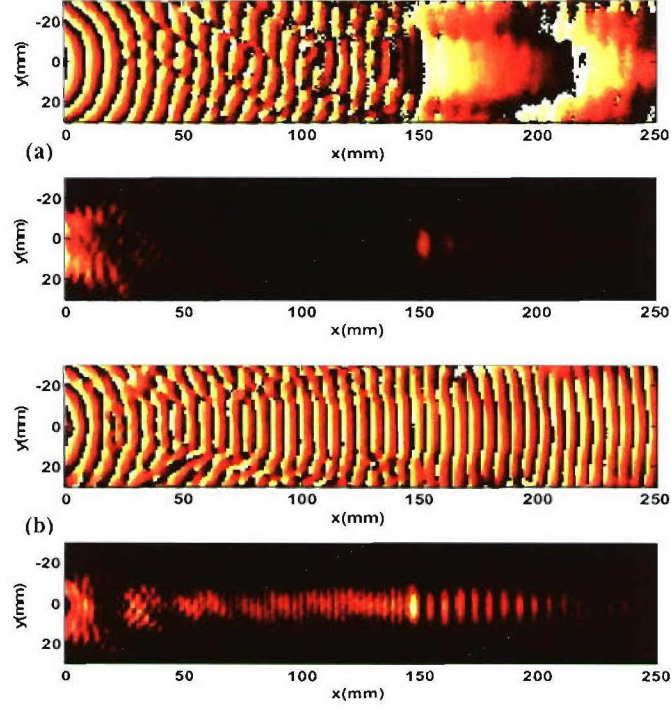

Fig. 12: Field distribution along the surface of the structure (xy plane). (a) The detector is 7mm over the surface. (b) The detector is 2mm over the surface.

2.3 SELF-COLLIMATION IN A 3D PHOTONIC CRYSTAL

The demonstration of self-collimation in 2D PhCs[38,29,68], provides a significant guiding approach, where nevertheless the vertical confinement of light is still achieved by index guidance. Numerical investigations of self-collimation in 3D PhCs were firstly reported in Refs. 69 and 70, and recently in Refs. 71 and 72, offering tantalizing new evidence that self-collimation in 3D PhCs should be possible, and opening the door to producing a totally new category of materials, namely "non-diffractive materials". However, no experimental work has been reported to date. If the significance of demonstration of self-collimation in 2D planar structures lies in providing a novel guiding approach, then the significance of demonstration of 3D self-collimation lies in opening the door to a completely new category of materials, namely "non-diffractive materials". The challenges are mostly attributable to the difficulty of 3D structure fabrication, and 3D field distribution measurement. As far as we know, there has never been experimental work reported to measure field distribution *inside* a 3D PhC at all. In this work, we have overcome these challenges. Herein, we demonstrate a 3D PhC as a new material, in which light can propagate *without divergence* while no specific route is introduced. A 3D PhC with desired dispersion was fabricated, and self-collimation was experimentally verified by mapping the field distribution *inside* the volume of the 3D PhC.

(a)   (b)
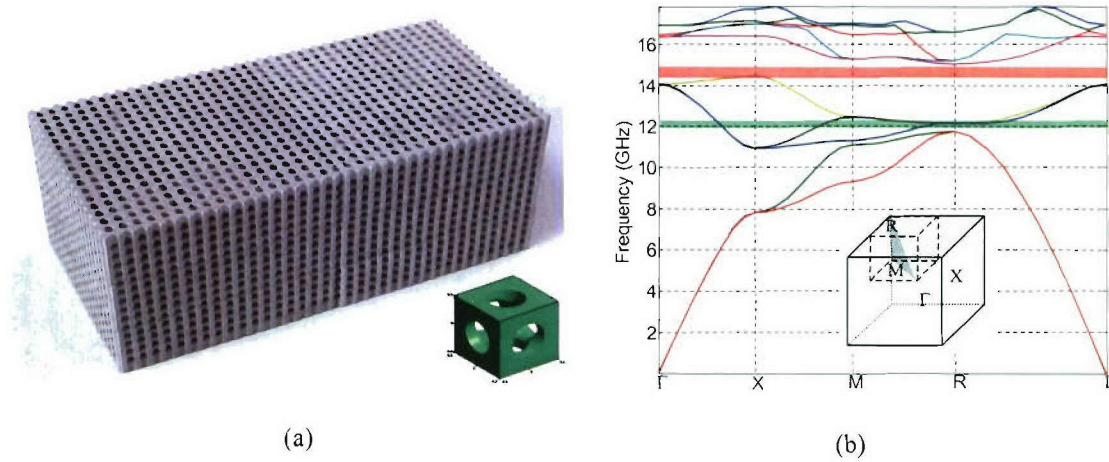
Fig. 13: (a) The simple cubic PhC fabricated by a high precision computer-controlled machine. It has 18×15 ×36units. (b) The photonic band diagram for the PhC.

Fig. 13(a) shows the 3D PhC we employed in this work. It is a simple cubic lattice with the unit cell shown in the inset. The hole diameter is $2r$=3.2mm, the lattice constant is a=5.0mm and the microwave material has a dielectric constant ϵ_r=30 (HiK500F, obtained from Emerson & Cumming). The overall dimensions are W85mm×H76mm×L170mm. The propagation of electromagnetic waves in a PhC is governed by Maxwell's equations with the periodic boundary condition defined by the PhC structure. In designing the structure, we used a plane-wave expansion method[3,73] to solve the Maxwell's equations and obtain the eigenvalues of frequency f for a given wavevector **k**. Fig. 13(b) shows the f-**k** diagram around the perimeter of the irreducible first Brillouin zone, also called the photonic band diagram. According to the diagram, a small bandgap appears between 14.4GHz and 15.0GHz, but that is not our center of attention. Instead, we focus on a frequency region centered at 12.3GHz, where self-collimation is expected. Fig. 14(a) shows the equi-frequency surfaces (EFSs) [30, 74] at 12.3GHz, which connect the

corresponding wavevector **k** values with eigenvalue f=12.3GHz. Notice that the EFSs are depicted in k-space and two degenerate bands exist. The third and fourth bands are shown in red and blue, respectively (The third band is also depicted separately in Fig. 14(b)). Since group velocity (and hence the direction of power flow) is calculated by the gradient of frequency in k-space, i.e., $\mathbf{v}_g = 2\pi\nabla_k f(\mathbf{k})$, power propagation direction is perpendicular to the EFSs. Although two bands are degenerate, both EFSs are nearly flat and, hence, 3D self-collimation modes are supported.

(a)   (b)

(c)
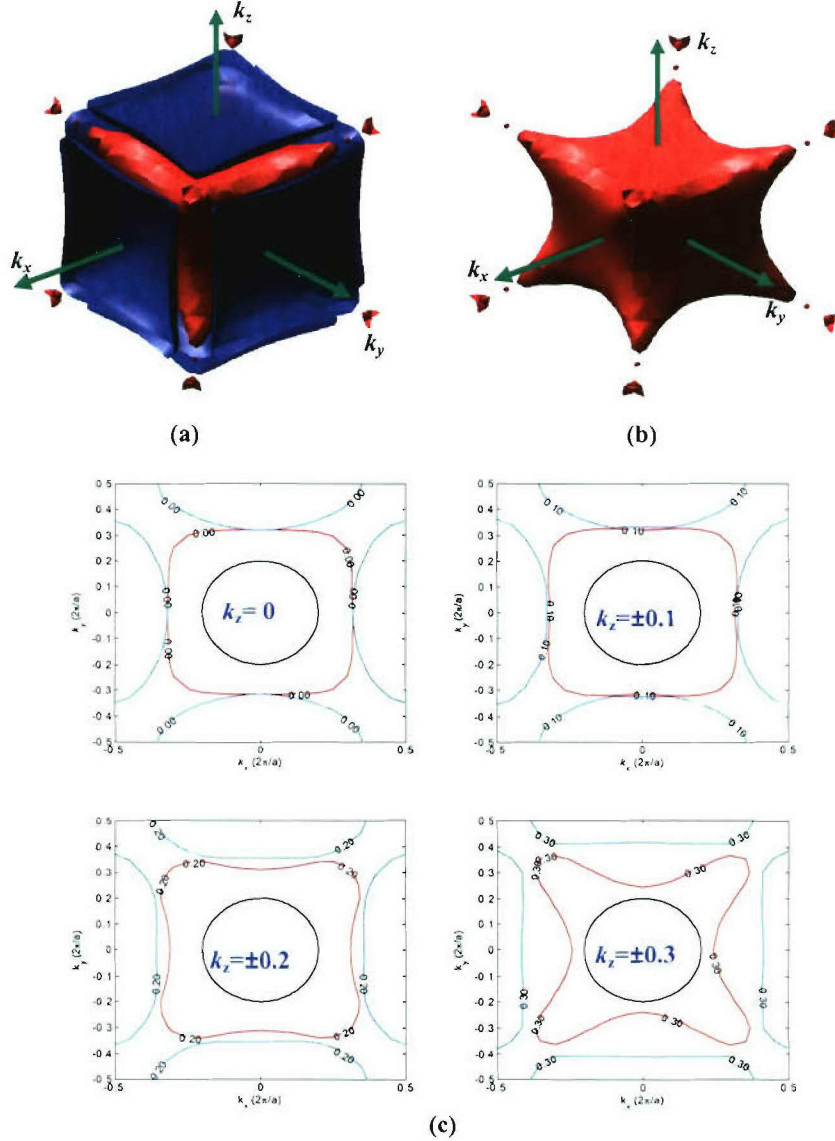
Fig. 14: (a) The equi-frequency surfaces for frequency f=12.3GHz. The third and fourth bands are degenerate. (b) The equi-frequency surface of the fourth band. (c) The equi-frequency surfaces shown as a series of contours for different k_z components. The black circle on each diagram is the dispersion contour for air.

18

A high precision computer controlled machine was employed to fabricate devices for microwave and millimeter-wave applications[25,26,67,68]. This 3D simple cubic PhC was fabricated by drilling aligned holes along the three orthogonal axes in six 85mm×85mm×25mm pieces of the dielectric material. These pieces were aligned and stacked to form the complete PhC. The fabrication precision was controlled to ±0.1mm, which is very small compared with the lattice constant and the wavelength of electromagnetic waves we will use. To perform the experiment, we established a 3D microwave imaging system[67]. The detector, a monopole 1.8mm in diameter with a 1-mm length of core exposed at the end, was mounted on an XYZ scanner. The fixed source was a waveguide with a flat copper ground plane at the end, and electric component polarized along the vertical axis. This configuration of the source is equivalent to a magnetic dipole source[75], which can excite the self-collimation modes in the third band. The source and the detector were connected to a vector network analyzer, through which the electric field distribution can be measured at any given point. A custom program was developed to synchronize the motion of the detector and the measurement of the corresponding field distribution. The diameter of the detector (1.8mm) is smaller than that of the holes (3.2mm). So we can insert the detector into the holes to map the field distribution inside all holes of the PhC following a point-by-point and hole-by-hole process. The presence of the detector introduces a defect, which will disturb the guiding route defined by linear boundaries, e.g. defect-guiding. However, in this case the guiding route is defined by the widely spreading periodicity of the PhC. Its influence on the field distribution is negligible. This is also verified by the experimental results presented in the following text.

In our experiment, we varied the frequency from 11.0GHz to 17.0GHz at intervals of 0.1GHz, and measured the electric field at 75 points along the length of each hole separated by 1.0mm steps. As a result, the electric field amplitude distribution was obtained as a 3D matrix with X75×Y17×Z34 elements[76] for each frequency. To estimate the beam size within the PhC, we used a standard definition of full width at half maximum (FWHM), where we reduced the effect of random variation by averaging the five highest values in each xy slice as the reference maximum value of that slice. To show the change of the beam size along the propagation direction, we determined the half-maximum of the intensity in each xy slice along the z-axis and rendered all of the half-maximum intensity contours as a 3D surface. As a result, the beam profile along the length of the PhC is indicated by the enclosed part of the 3D surface. Fig. 15(a) shows the beam profile at f=12.2GHz, which is a narrow, collimated beam. The intensity distributions of slices located at z=15mm and z=165mm are also shown in the insets of Fig. 15(a), respectively.

We calculated the beam diameters on all slices along the z-axis, and depicted them in Fig. 15(b). Curve fitting shows that the diameter of the beam increases 2mm (from 8.5mm to 10.5mm) at the propagation distance of 165mm. Close examination reveals the increase is mostly due to a jump at z=80mm, where considerable lattice misalignment exists. Optimizing the fabrication accuracy will improve the self-collimation. In contrast, at the same propagation distance a Gaussian beam[77] (with the waist size=8.5mm) theoretically expands its waist into 150mm in the air and 29mm in a material with ϵ_r=30, which are shown in Fig. 15(b) as the red and blue curves, respectively

Detailed analysis demonstrated that this self-collimation phenomenon was observed in the frequency range 12.1GHz~12.9GHz, consistent with the flat EFSs calculated for the third dispersion band at these frequencies. For comparison, we repeated the same measurement and analysis for the electromagnetic wave propagation in the air by removing the PhC while keeping all other instruments and their states. Supplement 3 shows a divergent beam profile in the air when the source is set at f=12.2GHz. The discrepancy of the profiles from ideal divergent beams is due to the reflection from environments. No collimated beam in the air is observed at any frequency in the range we measured. Therefore, the comparison of Fig. 15(a) and Supplement 3

further confirms that it is the presence of 3D PhC that results in the collimation of electromagnetic beam. In other words, the PhC cancels the diffraction effect and functions as a "non-diffractive material".
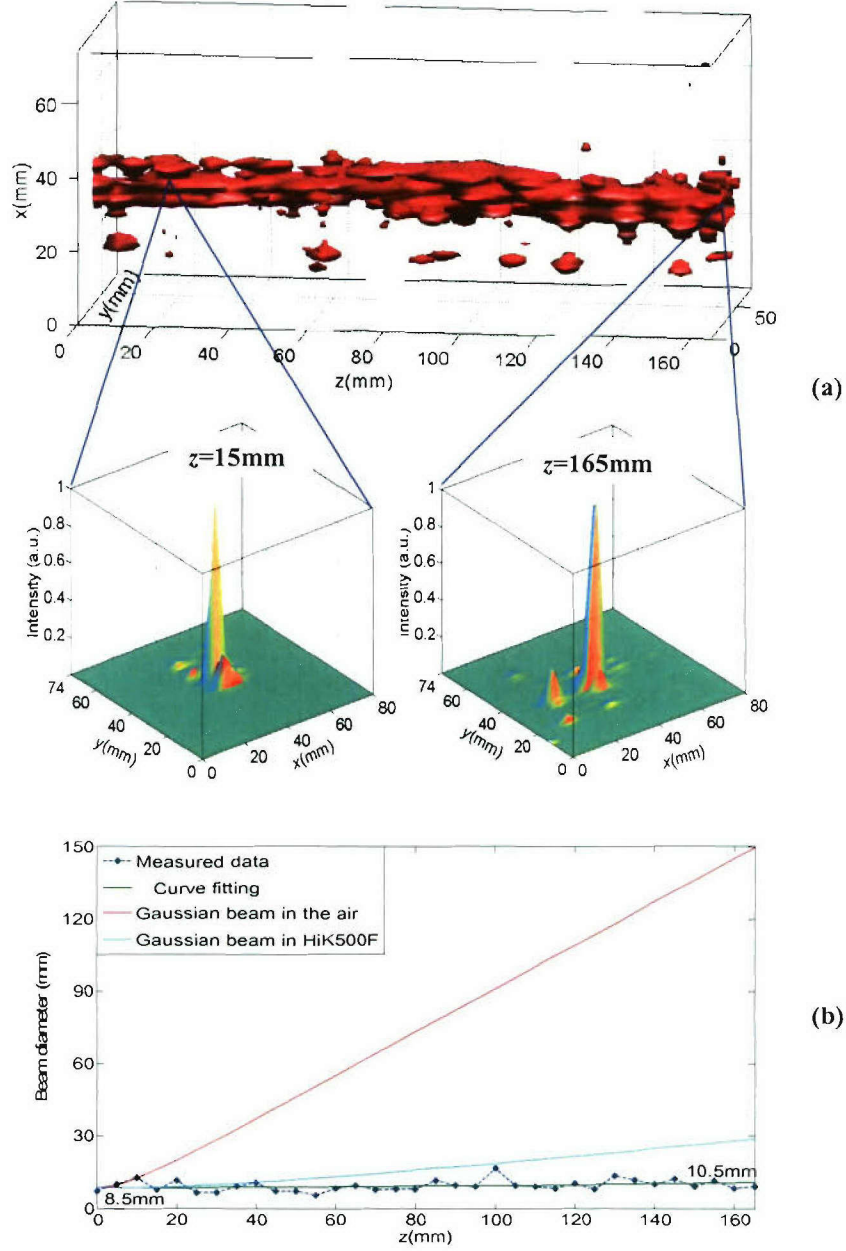

Fig. 15: (a) The FWHM beam profile in the PhC at f=12.2GHz. (b) The evolution of beam diameter in the PhC and common materials.

To observe how power is transported inside the PhC, we integrated the intensity over the first xy slice and used it as input power, and the last slice as output power. The propagation attenuation in the PhC can be calculated as the ratio between output and input. For different frequencies, we obtained different attenuations. Fig. 16(a) shows the relationship between the attenuation and

frequency. From this diagram, one can see that the largest attenuation (79dB) occurs inside bandgap (15.1GHz) while the smallest attenuation (15dB) occurs when the beam is self-collimated (12.4GHz). Green and red shaded bars indicate the minimum and maximum attenuation regions, respectively, which also coincide the self-collimation and bandgap ranges, respectively. In bandgap ranges, most of power dies out in the first several lattices. In the self-collimation, the power (in dB) decays approximately linearly along the z-axis, as shown in Fig. 16(b), except for considerable insertion loss in the coupling process. Similar issue also occurs in 2D self-collimation which was reported in Ref. 78. This may be solved by index matching or other novel approaches.

(a)   (b)
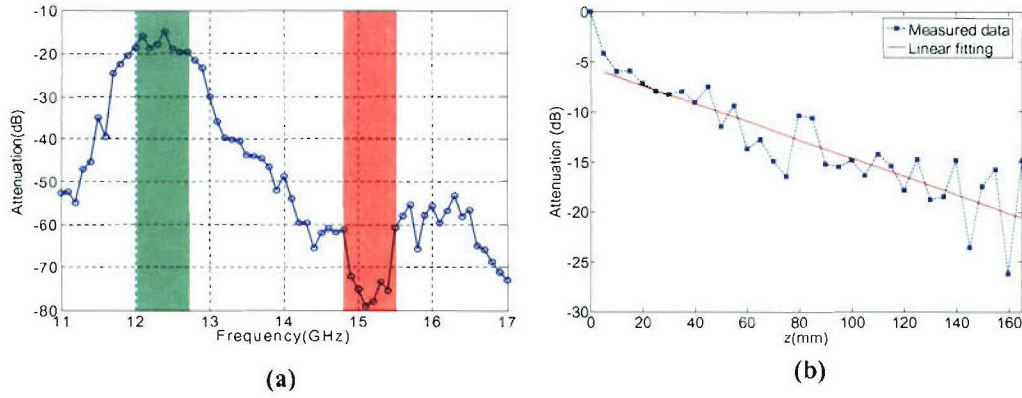
Fig. 16: (a) The relationship between the attenuation and working frequency. (b) The attenuation along the z-axis at f=12.4GHz.

2.4 HYBRID LATTICE PHOTONIC CRYSTAL CHANNELIZERS

Among the properties of photonic crystals, the unique dispersion and the bandgap are two representative characteristics that allow for designing devices by engineering the dispersion property or introducing point- and line-defects into PhCs. The dispersion property offers the electromagnetically transparent property and thereby significantly reduced the scattering cross-sections of devices. On the other hand, the bandgap property provides various functional devices, including channelizers, correlators, and filters. Generally, these devices are based on a single lattice or single property, such as line-defect waveguides based on a triangular lattice, and self-collimation based on a rectangular lattice. However, for the goal of eventually incorporating of different photonic crystal based devices into subsystems or systems, hybrid of different lattices is an essential task. In particular, it enables one to design more complex devices by combining different properties of the PhCs. Therefore, we proposed and demonstrated devices based on the combination of these two approaches that allow for both low scattering cross-section and functional devices.

The proposed hybrid lattice structure is based on the hybrid of the rectangular and triangular lattices of air holes on a slab, as shown in Fig. 17. The second pass band of the rectangular lattice is designed to be in the bandgap of the triangular lattice, as shown in Fig. 18.
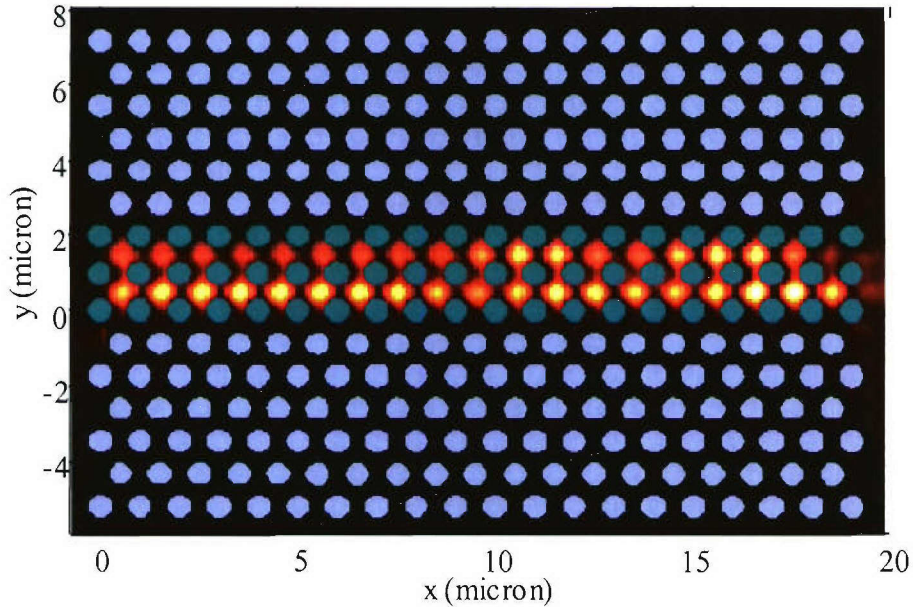
Fig. 17: The hybrid lattice structure with a rectangular lattice of air holes in the middle surrounded by a triangular lattice.

In this case, the triangular lattice is used both as an efficient boundary to confine light in the in-plane direction and as a base to introduce other devices such as cavities formed by point defects. On the other hand, the wave propagating in the rectangular lattice can be manipulated by designing its dispersion properties. Therefore, both the bandgap and the special dispersion property of the PhC are utilized in the structure. One straightforward application of this hybrid lattice structure is the low cross-section waveguide.
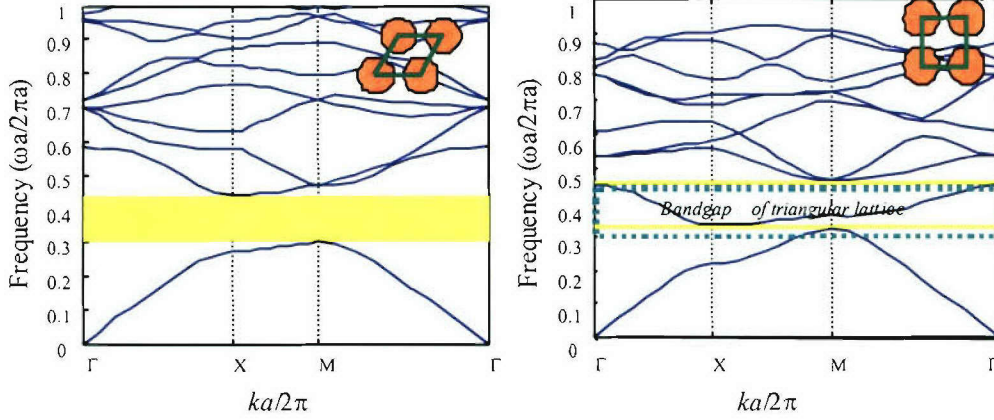
22

Fig. 18 : Dispersion diagrams of the triangular and rectangular lattices

To demonstrate the hybrid lattice waveguide, we first introduce the unique dispersion property of the photonic crystal. The dispersion surfaces of photonic cryatals gives one the ability to predict the direction of light propagating in a PhC by studying the shape of its equi-frequency surfaces (EFCs). Unlike ordinary materials which have ellipsoidal-shaped EFCs as shown in Fig. 19(a), PhCs can exhibit a wide variety of EFC shapes, which can be modified by manipulating the parameters of the PhC lattice, such as the lattice type, pitch, and fill-factor. If the EFC is a square-like shape, shown as the dashed line in Fig. 19(b), the directions of the group velocity are mostly limited to the two directions perpendicular to the square edges. If light is launched toward one edge of the EFC in a wide range of angles, it is only able to propagate in a narrow range of angles in the material. In this situation, light propagation in the PhC is self-collimated.
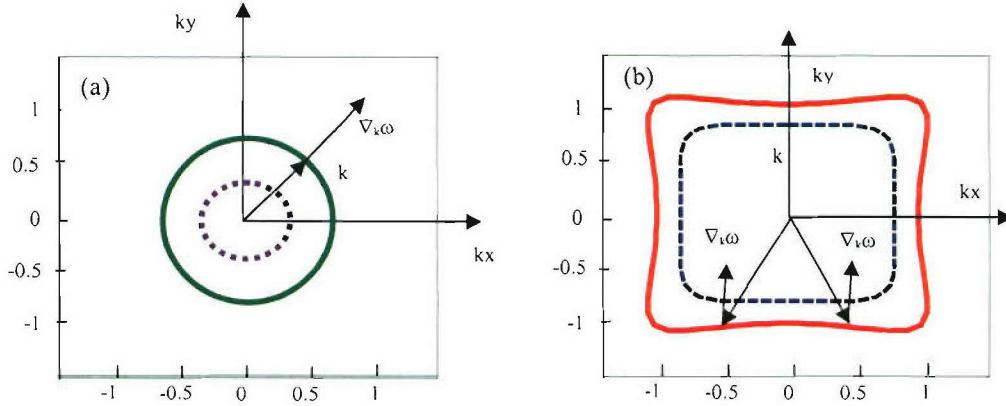
Fig. 19: EFCs of the rectangular lattice: (a) first band and (b) second band.

If EFCs were a perfect square, light would propagate in the photonic crystal without any divergence. However, EFCs have curved edges for real structures. As a result, the beam always diverges to some extent as it propagating in the lattice, as shown in Fig. 20. To deal with this problem, we created a hybrid lattice structure with a triangular lattice as the boundary to confine the light propagating in the rectangular lattice area. In this configuration, if the wavelength of light is in the bandgap of the triangular lattice, the divergent light, resulting from the curved edges of the EFCs, is reflected back to the waveguide. Therefore, the wave propagating in the

rectangular lattice is highly guided without divergence. In order to illustrate the efficiency of the hybrid structure, TE polarized waves enter a rectangular lattice and a hybrid lattice waveguide with the same length simulated using the 2D-FDTD method, as shown in Fig. 21.
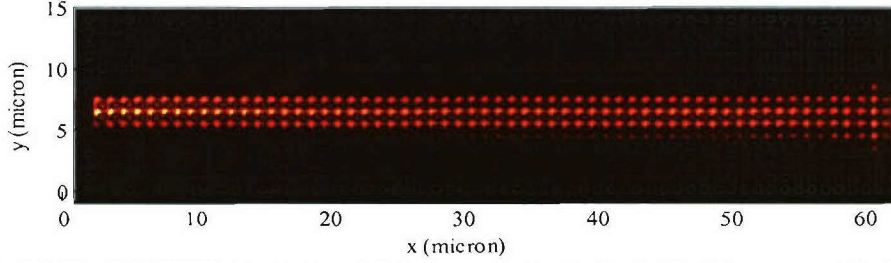

Fig. 20: The 2D-FDTD simulation of light propagating in the PhC with a square-like EFC.
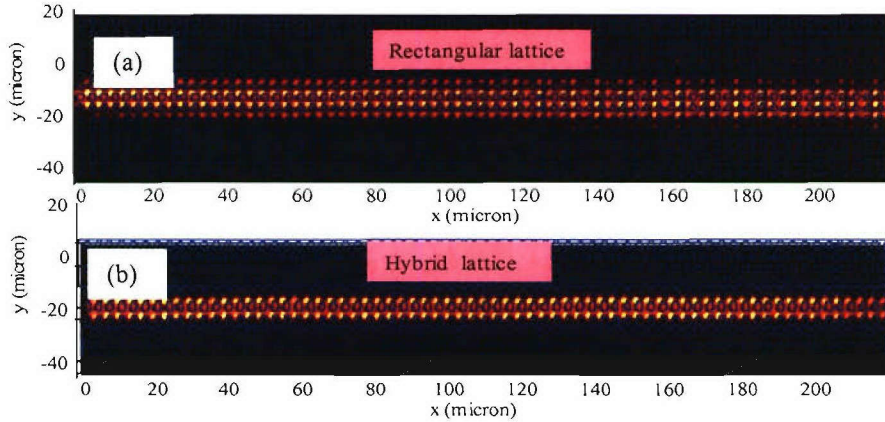

Fig. 21: The 2D-FDTD simulation of light propagating in the PhC with a square-like EFC.

For the hybrid lattice waveguide, the rectangular lattice with three periods in width is used as the waveguide. On each side of it is the triangular lattice serving as the boundary. In comparison to the single rectangular lattice, the hybrid lattice waveguide reveals better confinement by increasing the transmission of 20% within the propagation distance of 600 periods. This simulation results indicated the advantage of the hybrid lattice structure over single lattice structure by further increase the transmission. Moreover, if incorporating point defects into the triangular lattice, we can design wavelength selective devices, such as WDMs and channelizers.

The photonic crystal WDM in telecommunication wavelength has been demonstrated to reduce the device size hundreds and thousands of times more than currently used WDMs. In addition to this compactness, the motivation for using this type of demultiplexer is the possibility of integration with other PC devices on a single substrate, which makes them a potential candidate for communication systems, spectroscopy, and sensing. However, the high loss of the line-defect channel waveguide precludes its practical applications. Herein, we propose an alternative hybrid lattice PhC WDM device with a low-loss semi-self-collimated waveguide as the channel waveguide. In particular, the dropping characteristics are controlled by manipulating both the dispersion properties of the rectangular lattices and the parameters of the cavities. Therefore, this configuration is more favorable than general line-defect based WDMs, in which the dropping characteristics can only be controlled by manipulating the parameters of the

triangular lattice. To form the dropping channels, point defects in the vicinity of the channel waveguide are introduced in the triangular lattice region. In this configuration, if waves propagate in the channel with the frequencies coinciding with the resonance frequencies of the cavities, it might drop to the cavities, whereas the rest of the frequencies continue to propagate in the channel waveguide.

As in telecommunication applications, channelizers are important devices in millimeter-wave communication systems as well. Therefore, this design has been scaled to millimeter-wavelength in an attempt to design high-compact millimeter-wave communication devices. The hybrid lattice MMW channelizer is composed of two rows of rectangular lattice as the channel waveguide with the triangular lattices as the boundary. Both the rectangular and the triangular lattice are designed with the same lattice constant: $a = 9.7\ mm$ and $r/a = 0.35$, as shown in Fig. 23. Point defects are introduced to the triangular lattice as the dropping channels. The air-hole sizes around the cavities are adjusted to make the desired frequencies drop into different cavities.
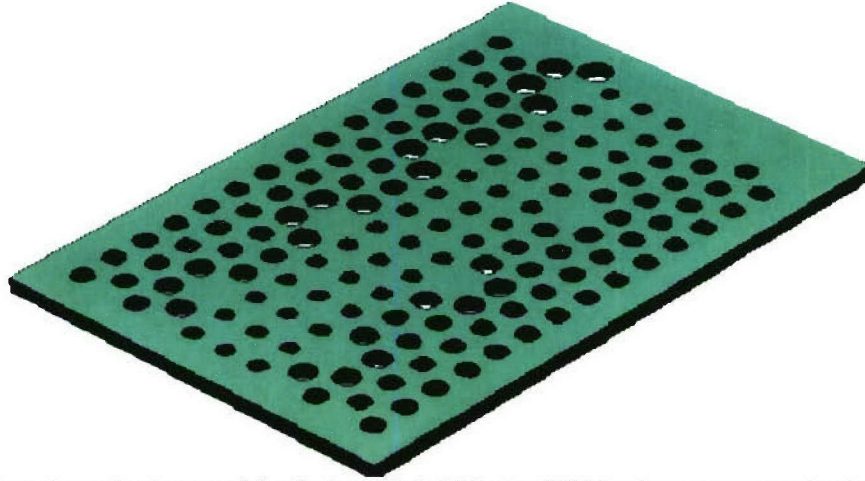
Fig. 22: The schematic picture of the designed hybrid lattice WDM, where a rectangular lattice serves as the channel waveguide and triangular lattices serve as the boundary. Point defects are introduced in the triangular lattice region as the cavities.

To experimentally validate it, the hybrid lattice PhC channelier was fabricated on a 2.4 mm thick HK 12 slab with a dielectric constant of 12.5 using a computer numerically controlled (CNC) machine. To simplify the structure for initial testing, the fabricated device only consisted of one dropping channel. The fabricated channelizer was characterized by using an Agilent 85106D network analyzer based system. A TE-polarized MMW with the wavelength swept from 10 GHz to 14 GHz was fed into the device. A monopole detector was used to map the surface of the device to detect the surface scattered field. The detected signals were feedback to the network analyzer and processed for the resulting of the surface scattered field pattern of the device. To verify the performance of the device, the measured results were compared with the 2D-FDTD simulation results, which are consistent with one another, as shown in Fig. 23. In both cases, the results show that with the 10.8 GHz wave entering, the wave drops to the cavity, whereas, with the 12 GHz wave entering, the wave propagates along the waveguide.
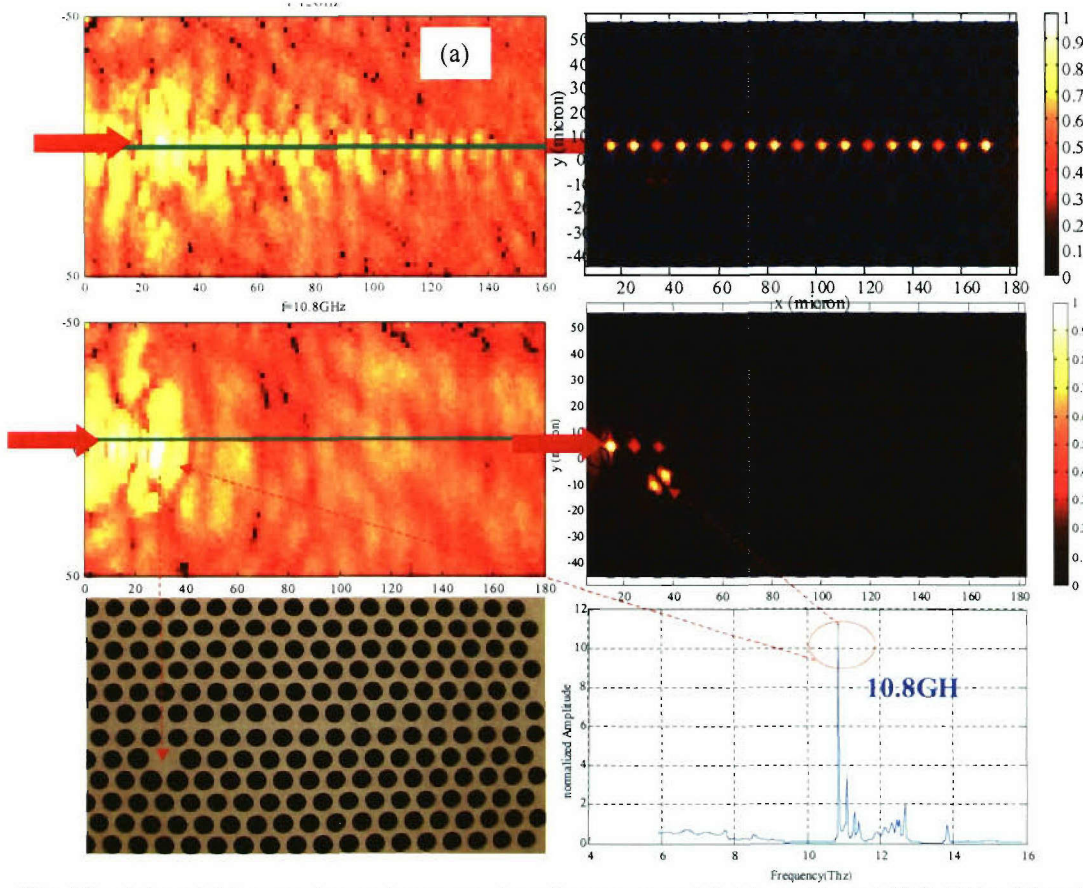
Fig. 23: (a) and (c), experimental measured surface-scattered fields at 12 and 10.8 GHz; (b) and (d), 2D-FDTD simulations of steady-state Hz fields at 12 and 10.8 GHz; (e), fabricated HLPWDM; (f), 2D-FDTD calculated transmission spectrum at the cavity.

To further study the mechanism of this hybrid lattice structure, we calculated the dispersion diagram, field, and phase distribution of this structure using the 2D-PWM method, shown in Fig.24. Multimodes show up in the bandgap, where 10.8 GHz frequency is belonged to a flat band, or a cavity mode. Meanwhile, the 12 GHz belongs to a guiding mode of the structure. The 2D-PWM simulation results are consistent with both the experimental and 2D-FDTD simulation results as shown in Fig. 23.

Encouraged by the promising experimental results, we designed a compact 1 × 4 channelizer with a size of 10λ using the 2D-FDTD method. The structure consists of a channel waveguide composed of two rows of rectangular lattice and drop channels formed by coupled cavities with different cavity sizes, as shown in Fig. 25(a). The coupled cavity channels are formed by the adjacent point defects to increase the dropping efficiency as well as to guide the dropped waves.

The resonant frequency of each channel is adjusted by increasing the radius of the air holes around the cavities as well as introducing reduced-size air holes into the cavities. Some of the radii of the air holes around the defects are enlarged to 8.1, 8.8, 9.1 and 8.2 mm respectively to ensure the resonant wavelengths for the respective channels are as 10.8, 11.1, 11.4 and 12.2 GHz, respectively. Fig. 25(b) shows the spectra detected at each branch channel with the detectors

placed in them. The sharp peaks presented at the spectra indicate these wavelengths are dropped into their respective branch channels from the channel waveguide.
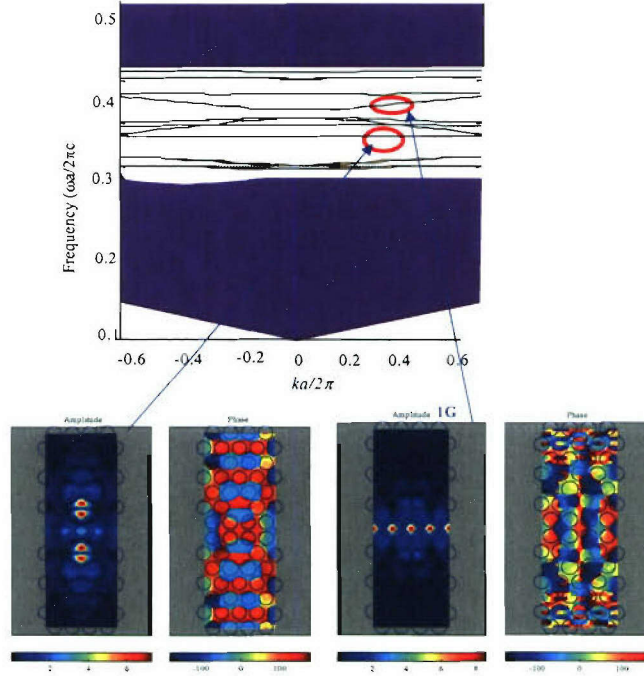
Fig.24: 2D-PWM calculation of the dispersion diagram of the hybrid lattice, structure field patterns, and phase at the 10.8 and the 12 GHz.
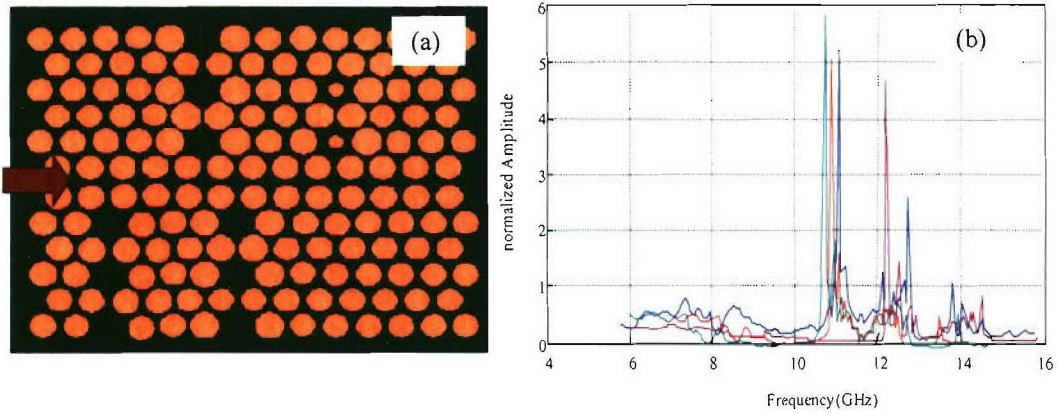

Fig. 25: Schematic of the 1 × 4 WDM based on the hybrid lattice.

To validate the design, the structure is simulated with a TE-polarized wave coupling into the rectangular lattice channel waveguide. The steady state results are consistent with the spectra. The desired wavelengths are dropped to their respective channels, shown in Fig. 26. The simulation and experimental results clearly demonstrated the ability of the proposed device to drop different frequencies from a channel waveguide to multiple channels. Based on the same mechanism, multichannel demultiplexers can be realized with careful design of the dispersion surface of the rectangular lattice and the parameters of the cavities.

Using a rectangular lattice as the channel waveguide for this hybrid lattice WDM has several advantages in addition to the ultra-small size. First, it gives more freedom for designing more efficient and complex functional devices by engineering both the point defects and the dispersion surfaces of the lattices. In addition, the similarity between the hybrid structures and the CROW structures proposed by S. Fan's group for light-stopping devices may suggest a new way to realize the phenomenon. Interestingly, if the wavelength is within both the bandgaps of the triangular and rectangular lattices, light can be trapped in the cavity resulting in high Q-value of the cavity and a long lifetime for the defect modes. Finally, since coupling is very sensitive to both the lattice and cavity parameters, it is very easy to control the adding/dropping of desired frequencies by incorporating nonlinear materials into the structure.
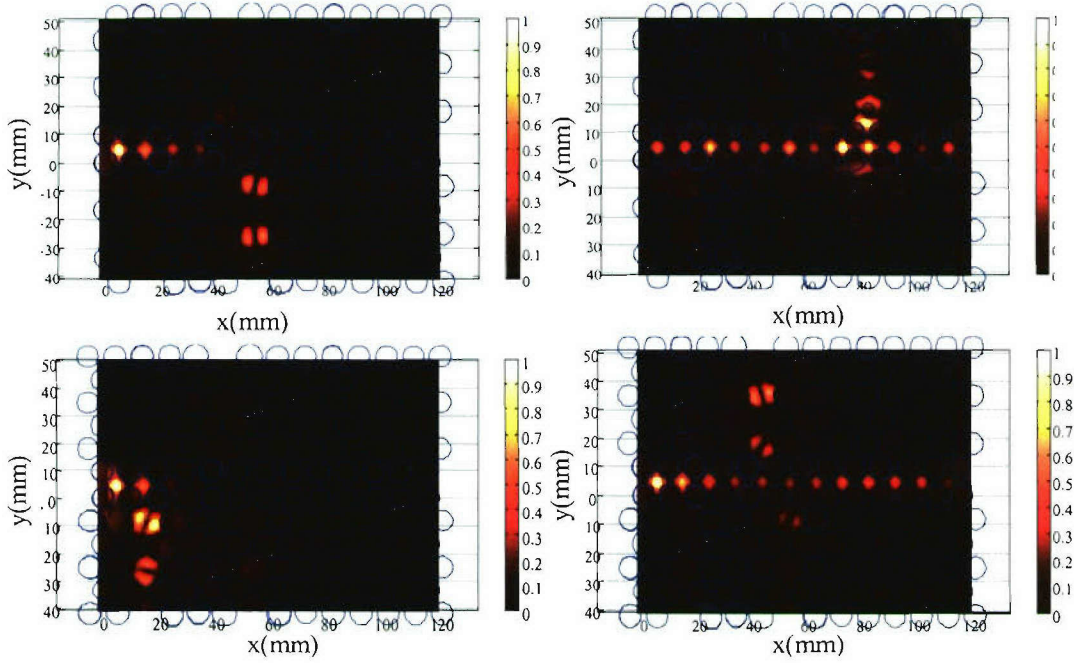
Fig. 26: 2D-FDTD calculated steady state Hz fields of 1 × 4 hybrid lattice PhC WDM with the 10.8 GHz, 11.1 GHz, 11.4 GHz, and 12.2 GHz wavelengths of light dropped at different channels.

As demonstrated, PhCs provide a great opportunity to implement various wavelength selective devices, including channelizers. These devices are based on 2D photonic crystals, wherein the waves enter the slab in-plane. However, with the wave entering the slab out-of-plane, the transmission spectrum exhibits guided resonance phenomenon that is significantly different from the well-studied in-plane incident cases. Herein, we present a displacement tunable filter based on this guided resonance phenomenon.

Most studies of 2D-PhCs are focused on light that is confined in PhC slabs or propagating in-plane of the slabs. Relatively little research has been devoted to studying light normally incident to a PhC slab, in which the observed phenomena are significantly different from the well-studied in-plane/parallel incident cases. A typical feature of a case in which light is normally incident is the transmission spectrum characterized by the sharp "Fano-like" resonance feature, or the guided resonance, which was introduced by S. Fan's group at Stanford University. Unlike usual guided modes, in which light is confined within the slab, guided resonances provide a unique way to

channel light from within the slab to the external environment. Conversely, light can be coupled into the device through the PhC as well. Furthermore, the sharp Fano-like guided resonance peaks offer a simple yet efficient way to implement wavelength selective devices, such as sensitive filters, which are key elements in satellite, mobile, wireless, microwave, and millimeter-wave communication systems. In addition, if two PhC slabs are combined, they form a sensitive displacement-tunable structure that can be utilized in designing functional tunable devices, such as switches, filters, modulators, and sensors. The key feature of this tunable device is its compaction and sensitivity due to the small mechanical motion required for device operation.

(a)   (b)
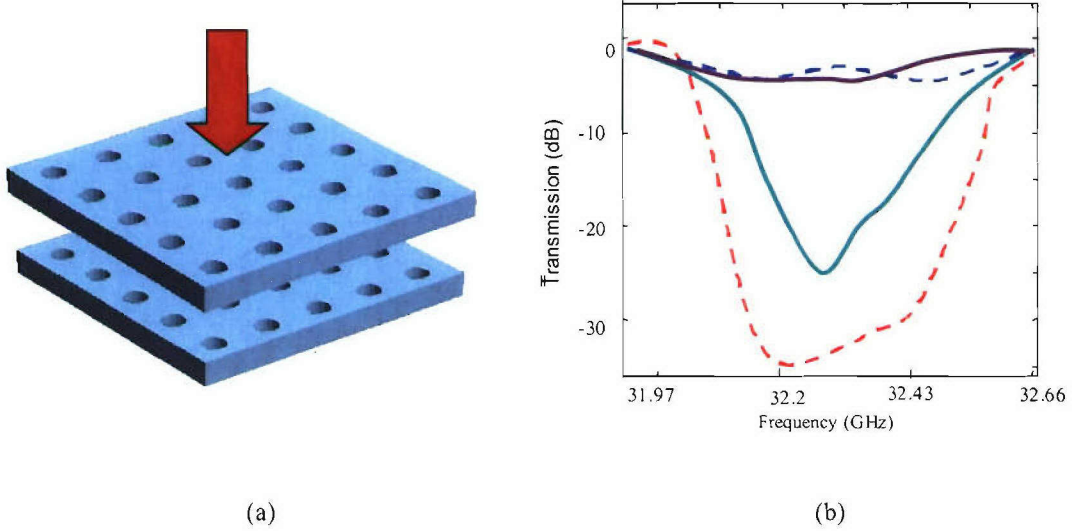
Fig. 27: (a) Schematic picture of a displacement sensitive PhC filter. (b) Experimentally measured transmission spectra of the GRF; dashed and solid lines represent the measured and 3D-FDTD calculated transmission spectra, with the red and the green curves represent the gap as 3mm, blue and purple represent the 1mm gap, respectively.

However, most of the studies on the guided resonance are concentrated on theoretical simulations. We demonstrated a displacement tunable filter, shown in Fig. 27(a). We simulated and experimentally measured the transmission spectra of this structure using the 3D-FDTD method and the same measurement setup for measuring single-slab based guided resonant filters. The slabs are the same as in the single-slab case, in which the PhC consists of a square lattice of air holes with $a = 3.3$ mm and $r = 1$ mm. The measurement is conducted after the distance between the slabs is changed from 1 mm to 3 mm, which is in the sub-wavelength range. Fig. 27(b) shows the measured and the 3D-FDTD calculated transmission spectra of this tunable filter; the dashed lines represent the measured spectra and the solid lines display the 3D-FDTD calculated results. The red and green curves representing the transmission spectra with the distance between the two slabs equals to 1 mm, whereas the purple and blue curves representing the spectra with the distance between the slabs is increased to 3 mm. From these spectra, one can observe that the wave totally transmitted at 3 mm and highly reflected at 1 mm. Furthermore, the 30dB drop rate is very promising for various applications, including sensors.

3.0 DISCUSSION AND CONCLUSION

To summarize, we designed, fabricated PhCs for millimeter applications and experimentally demonstrated, for the first time, self-collimation effect using both amplitude and phase, for low index contrast photonic crystals. Theoretically, for high index contrast photonic crystals self-collimation is easier to be achieved because it is easier to engineer the EFCs to desired shape and it is easier to avoid band degeneracy. Consequently, we can conclude that self-collimation is a very widely existing phenomenon for PhCs and a new guiding and routing mechanism for various applications. This work also clarified two different guiding mechanisms of PhCs, namely "bandgap plus defects" and self-collimation, because there is no bandgap at all in our PhCs. Due to fewer limitations for index contrast materials, this new guiding and routing mechanism will play a more important role in optical integration and millimeter-wave communications as we expected. In millimeter-wave regime, the possible development of narrow beam maintenance for acceptable size would enable better tracking, detection and surveillance in modern radars and antennas.

In addition, we proposed the use of the unique dispersion property of photonic crystals, namely self-collimation, to supply a good feeding wave for a dielectric-grating antenna. With the integration of such a photonic crystal, we designed and fabricated a millimeter-wave grating antenna. In the experiment, we characterized the device by observing the near field distribution of the integrated device. Experimental results showed that self-collimation photonic crystal is a good candidate for feeding the grating antenna. Both the photonic crystal and the grating antenna have compact dimensions, which make them easily integrated with other planar devices. In many applications the use of navigation and communication waveguides and antennas renders an otherwise structurally sound platform at risk of being compromised. However, the antenna system we developed preserves the structural integrity of naval platforms as a well as maintain low scattering cross-sections.

Furthermore, a 3D simple cubic PhC was fabricated and its dispersion properties were investigated. Experiments demonstrated 3D self-collimation in the PhC by mapping 3D field distribution inside the PhC. This is the first time that a "non-diffractive material" based on 3D PhC has been fabricated and characterized. Therefore, these results have both theoretical and application significance, and constitute a breakthrough toward the development of novel electromagnetic materials.

Finally, we experimentally validated hybrid lattice waveguides, channelizers, and displacement tunable filters. The demonstration of the hybrid lattice wavelength selective devices indicated that this hybrid lattice structure is not only a potential candidate for filter and channelizer applications, but also opens a new direction for designing devices by utilizing a combination of different properties and lattices of PhCs. In addition, we presented displacement tunable filters for filter, sensor, and switch applications. The demonstration of channelizers and displacement filters suggested that these ultra-small size devices have great potential in developing millimeter-wave signal processing systems with wide bandwidth and high processing capabilities. These results offer opportunities in designing sensors with the directly signal processing abilities. To this end, we will continue our work on developing high-speed, compact and low cost millimeter-wave signal processing devices and systems.

4. Publications for This Program

Journal Publications:

1. Z. Lu, S. Shi, J. A. Murakowski, G. J. Schneider, C. A. Schuetz, and D. W. Prather, "Experimental demonstration of self-collimation inside a three-dimensional photonic crystal," *Physical Review Letters*, vol.**96**, No.17, 173902(4) (2006). †

2. Z. Lu, C. Chen, C. A. Schuetz, S. Shi, J. A. Murakowski, G. J. Schneider, and D. W. Prather, "Sub-wavelength imaging by a flat cylindrical lens using optimized negative refraction," *Applied Physics Letters*, vol. **87**, No.9, 091907(3) (2005).

3. Z. Lu, S. Shi, J. A. Murakowski, G. J. Schneider, C. A. Schuetz, and D. W. Prather, "Experimental demonstration of self-collimation inside a three-dimensional photonic crystal," *Physical Review Letters*, vol.**96**, No.17, 173902(4) (2006). ‡

4. Z. Lu, C. A. Schuetz, S. Shi, C. Chen, G. P. Behrmann, and D. W. Prather, "Experimental demonstration of self-collimation in low index contrast photonic crystals in the millimeter-wave regime," *IEEE Transactions on Microwave Theory and Techniques*, vol.**53**, No. 4, 1362-1368(2005).

5. Z. Lu, S. Shi, C. A. Schuetz, J. A. Murakowski, and D. W. Prather, "Three-dimensional photonic crystal flat lens by full 3D negative refraction," *Optics Express*, vol.**13**, No.15, 5592-5599 (2005).

6. Z. Lu, S. Shi, C. A. Schuetz, and D. W. Prather, "Experimental demonstration of negative refraction imaging in both amplitude and phase," *Optics Express*, vol.**13**, No.6, 2007-2012(2005).

7. Z. Lu, J. A. Murakowski, C. A. Schuetz, S. Shi, G. J. Schneider, and D.W. Prather, "A perfect lens makes a perfect trap," *Optics Express* vol.**14**, No.6, 2228-2235 (2006). ▲

8. C Lin, Z. Lu, S. Shi, G. Jin, and D. W. Prather, "Experimentally demonstrated filters based on guided resonance of photonic crystal films," *Applied Physics Letters*, vol. **87**, 091102(3) (2005).

9. C. Chen, Z. Lu, S. Shi, and D. W. Prather, "Self-guiding in low-index-contrast planar photonic crystals," *International Journal of High Speed Electronics and Systems*, vol. **14**, No. 3, 720-725, 2004.

† Selected by *The Virtual Journal of Nanoscale Science & Technology*, vol. **12**, No. 16, Oct. 17, 2005: http://scitation.aip.org/dbt/dbt.jsp?KEY=VIRT01&Volume=12&Issue=16

‡ Selected by *The Virtual Journal for Biomedical Optics*, vol. **1**, No. 4, Apr. 2006: http://vjbo.osa.org/browse.cfm?journal=17&volume=,1&issue=,1-4

▲ Selected by *The Virtual Journal for Biomedical Optics*, vol. **1**, No. 4, Apr. 2006: http://vjbo.osa.org/browse.cfm?journal=17&volume=,1&issue=,1-4

Conference Publications and Presentations:

1. Z. Lu, S. Shi, C. A. Schuetz, C. Lin, C. Chen, A. S. Sharkawy, and D. W. Prather, "Photonic crystal planar lens working at low frequencies," *Proc. of SPIE,* vol. **5733**, *Quantum Sensing and Nanophotonic Devices II*, pp.444-449 (2005).

2. Z. Lu, C. Schuetz, C. Chen, S. Shi, and D. W. Prather, "Micromilled dielectric PBG self-collimation devices in millimeter-wave regime," *USNC/URSI National Radio Science Meeting*, Monterey, CA, June 20-25, 2004.

3. Z. Lu, S. Shi, and C. A. Schuetz, and D. W. Prather, "Design, fabrication, and characterization of engineered materials in the microwave and millimeter-wave regime," *IEEE AP-S International Symposium and USNC/URSI National Radio Science Meeting*, Washington, DC, July 3-8, 2005.

4. Z. Lu, S. Shi, J. A. Murakowski, C. A. Schuetz, G. J. Schneider, and D. W. Prather, "Experimental demonstration of self-collimation in 3D photonic crystal at microwave frequencies," *Photonics West*, Photonic Crystal Materials And Devices IV, San Jose, CA, Jan., 2006.

5. D. W. Prather, S. Shi, S. Venkataraman, Z. Lu, J. Murakowski, and G. Schneider, "Self-collimation in 3D photonic crystals," *Proc. of SPIE,* vol. **5733**, *Quantum Sensing and Nanophotonic Devices II*, pp. 84-93 (2005).

6. D. W. Prather, Z. Lu, S. Shi, and C. A. Schuetz, "Dispersion engineering for 3D subwavelength imaging using photonic crystals," *Photonics West*, Photonic Crystal Materials And Devices IV, San Jose, CA, Jan., 2006.

7. D. W. Prather, Z. Lu, J. A. Murakowski, S. Shi, G. J. Schneider, C. A. Schuetz, P. Yao, and B. Citla "Design, fabrication, and application of three dimensional dispersion engineered photonic crystal devices," *Integrated Photonics Research and Applications and the Nanophotonics Topical Meetings (IPRA/NANO)*, Uncasville, CT, Apr., 2006.

8. D.W. Prather, Z. Lu, J. A. Murakowski, C. A. Schuetz, S. Shi, and G. J. Schneider, "A perfect lens makes a perfect trap," *CLEO/QELS '06*, Long Beach, CA, May, 2006.

9. D. W. Prather, Z. Lu, J. A. Murakowski, S. Shi, C. Chen C. A. Schuetz, and G. J. Schneider, "Subwavelength imaging by full 3D negative refraction using a 3D photonic crystal," *Photonic Metamaterials: From Random to Periodic Topical Meeting*, The Bahamas, Jun., 2006.

5. Table of Figures

References and Notes

[1] E. Yablonovitch, "Inhibited spontaneous emission in solid-state physics and electronics," *Phys. Rev. Lett.* **58**, 2059-2062 (1987).

[2] S. John, "Strong localization of photons in certain disordered dielectric superlattices," *Phys. Rev. Lett.* **58**, 2486-2489 (1987).

[3] K. M. Ho, C. T. Chan, and C. M. Soukoulis, "Existence of a photonic gap in periodic dielectric structures," *Phys. Rev. Lett.* **65**, 3152-3155 (1990).

[4] E. Ozbay, *et al.* "Measurement of three-dimensional photonic band gap in a crystal structure made of dielectric rods," *Phys. Rev. B* **50**, 1945-1948 (1994).

[5] Krauss, T. *et al.* "Two-dimensional photonic bandgap structures operating at near-infrared wavelengths," *Nature* **383**, 699-702 (1996).

[6] S. John, "Localization of light," *Phys. Today* **May**, 32-40 (1991).

[7] S. Noda, A. Chutinan and M. Imada, "Trapping and emission of photons by a single defect in a photonic bandgap structure," *Nature* **407**, 608-610 (2000).

[8] A. Scherer, T. Yoshie, M. Loncar, J. Vuckovic and K. Okamoto, "Photonic Crystal Nanocavities for Efficient Ligh Confinrment and Emission," *J. of the Korean Physical Society* **42**, 768-773 (2003).

[9] S. Fan, P. R. Villeneuve, J. D. Joannopoulos, and H. A. Haus, "Channel drop tunneling through localized states," *Phys. Rev. Lett.* **80**, 960-3 (1998).

[10] S. Fan, P. R. Villeneuve, and J. D. Joannopoulos, "Channel drop filters in photonic crystals," *Opt. Express* **3**, 4-11 (1998).

[11] A. Sharkawy, D. Pustai, S. Shi, D. W. Prather, "High transmission through waveguide bends by use of polycrystalline photonic-crystal structures," *Opt. Lett.* **28**, 1197-1199 (2003).

[12] D. W. Prather, J. Murakowski, S. Shi, S. Venkataraman, A. Sharkawy, C. Chen, and D. Pustai, "High-efficiency coupling structure for a single-line-defect photonic-crystal waveguide," *Opt. Lett.* **27**, 1601-1603 (2002).

[13] A. Yariv, Y. Xu, R. K. Lee, and A. Scherer, "Coupled resonator optical waveguide: A proposal and analysis," *Opt. Lett.* **24**, 711-713 (1999).

[14] M. Bayindir, B. Temelkuran, and E. Ozbay, "Propagation of photons by hopping: A waveguiding mechanism through localized coupled-cavities in three-dimensional photonic crystals," *Phys. Rev. B* **61**, R11855-R11858 (2000).

[15] U. Peschel, A. L. Reynolds, B. Arredondo, F. Lederer, P. J. Roberts, T. F. Krauss, P. J. I. de Maagt, "Transmission and reflection analysis of functional coupled cavity components," *IEEE J. of Quantum Electron.* **38**, 830 – 836 (2002).

[16] A. L. Reynolds, U. Peschel, F. Lederer, P. J. Roberts, T. F. Krauss, and P. J. I. de Maagt, "Coupled defects in photonic crystals," *IEEE Trans. on Microw. Theory and Techniques* **49**, 1860 – 1867(2001).

[17] S. Y. Lin, E. Chow, V. Hietala, P. R. Villeneuve, and J. D. Joannopoulos, "Experimental Demonstration of Guiding and Bending of Electromagnetic Waves in a Photonic Crystal," *Science* **282**, 274-276(1998).

[18] M. D. B. Charlton, M. E. Zoorob, G. J. Parker, M. C. Netti, J. J. Baumberg, S. J. Cox and H. Kemhadjian, "Experimental investigation of photonic crystal waveguide devices and line-defect waveguide bends," *Mat. Sci. and Eng. B* **74**, 17-24(2000).

[19] S. Fan, S. G. Johnson, J. D. Joannopoulos, C. Manolatou, and H. A. Haus, "Waveguide branches in photonic crystals ," *J. Opt. Soc. Am. B* **18**, 162-165 (2001)

[20] A. Sharkawy, S. Shi, D. Prather, and R. Soref, "Electro-optical switching using coupled photonic crystal waveguides," *Opt. Express* **10**, 1048-1059 (2002).

[21] M. F. Yanik, S. Fan, M. Soljacic, and J. D. Joannopoulos, "All-optical transistor action with bistable switching in a photonic crystal cross-waveguide geometry," *Opt. Lett.* **28**, 2506-2508 (2003).

[22] O. Painter, R. K. Lee, A. Scherer, A. Yariv, J. D. O'Brien, P. D. Dapkus, and I. Kim, "Two-dimensional photonic band-gap defect mode laser," *Science* **284**, 1819-21 (1999).

[23] C. Chen, G. Jin, S. Shi, A. Sharkawy, and D. W. Prather, "A unidirectional photonic crystal dispersion-based emitter," *Appl. Phy. Lett.* **84**, 3151-3153 (2004).

[24] E. R. Brown, C. D. Parker, and E. Yablonovitch, "Radiation properties of a planar antenna on a photonic-crystal substrate," *J. Opt. Soc. Am. B* **10**, 404-407 (1993).

[25] Z. Lu, J. A. Murakowski, C. A. Schuetz, S. Shi, G. J. Schneider, and D. W. Prather, "Three-dimensional subwavelength imaging by a photonic-crystal flat lens using negative refraction at microwave frequencies," *Phys. Rev. Lett.* **95**, 153901(4) (2005).

[26] Z. Lu, C. Chen, C. A. Schuetz, S. Shi, J. A. Murakowski, G. J. Schneider, and D. W. Prather, "Sub-wavelength imaging by a flat cylindrical lens using optimized negative refraction," *Appl. Phys. Lett.* **87**, 091907(3) (2005).

[27] S. -Y. Lin, V. M. Hietala, L. Wang, and E. D. Jones, "Highly dispersive photonic band-gap prism," *Opt. Lett.* **21**, 1771-1773 (1996).

[28] H. Kosaka, T. Kawashima, A. Tomita, M. Notomi, T. Tamamura, T. Sato, and S. Kawakami, "Superprism phenomena in photonic crystals," *Phys. Rev. B* **58**, R10096-10099 (2000).

[29] H. Kosaka, T. Kawashima, A. Tomita, M. Notomi, T. Tamamura, T. Sato, and S. Kawakamib, "Self-collimating phenomena in photonic crystals," *Appl. Phys. Lett.* **74**, 1212–1214(1999).

[30] J. Witzens, M. Loncar, and A. Schere, "Self-collimation in planar photonic crystals," *IEEE J. Sel. Topics Quant. Electron.* **8**, 1246–1257(2002).

31 M. Soljacic, S. G. Johnson, S. Fan, M. Ibanescu, E. Ippen, and J. D. Joannopoulos, "Photonic-crystal slow-light enhancement of nonlinear phase sensitivity," *J. Opt. Soc. Am. B* **19**, 2052-2059(2002).

[32] A. Ashkin, J.M. Dziedzin, and P.W. Smith, "Continous-wave self-focusing and self-trapping of light in artificial Kerr media," *Opt. Lett.* **7**, 276-278(1982).

[33] S.Y. Lin, E. Chow, V. Hietala, P.R. Villeneuve and J.D. Joannopoulos, "Experimental demonstration of guiding and bending of electromagnetic waves in a photonic crystal," *Nature* **282**, 274-276(1998).

[34] M. Qi, E. Lidorikis, P.T.Rakich, S.G. Johnson, J.D. Joannopoulos, E.P. Ippen, and H.I. Smith, "A three-dimensional optical photonic crystal with designed point defects," *Nature* **429**, 538-542(2004).

[35] S. Ogawa, M. Imada, S. Yoshimoto, M. Okano, and S. Noda, "Control of light emission by 3D photonic crystals," *Science* **305**, 227-229(2004).

[36] P. St. J. Russell, "Interference of integrated Floquet-Bloch waves," *Phys. Rev. A* **33**, 3232-3242 (1986).

[37] S. Y. Lin, V. M. Hietala, L. Wang, and E. D. Jones, "Highly dispersive photonic band-gap prism," *Opt. Lett.* **21**, 1771-1773 (1996).

[38] D.W. Prather, S. Shi, D.M. Pustai, C. Chen, S. Venkataraman, A. Sharkawy, G. J. Schneider, and J.A. Murakowski, "Dispersion-based optical routing in photonic crystals," *Opt. Lett.* **29**, 50-52(2004).

[39] D. N. Chigrin, S. Enoch, C. M. S. Torres and G. Tayeb, "Self-guiding in two-dimensional photonic crystals, " *Opt. Express* **11**, 1203-1211 (2003).

[40] C. Chen, A. Sharkwy, S. Shi, and D. W. Prather, Integrated Photonics Research, *OSA Technical Digest* (Optical Society of American, Washington DC, 2003), p-39.

[41] X. Yu and S. Fan, "Bends and splitters for self-collimated beams in photonic crystals," *Appl. Phys. Lett.* **83**, 3251-3253 (2003).

[42] D. M. Pustai, S. Shi, C. Chen, A. Sharkawy, and D.W.Prather, "Analysis of splitters for self-collimated beams in planar photonic crystals," *Opt. Express* **12**, 1823-1831 (2004).

[43] D. W. Prather, S. Shi, D. M. Pustai, C. Chen, S. Venkataraman, A. Sharkawy, G. J. Schneider, J. Murakowski, "Dispersion-based optical routing in photonic crystals," *Opt. Lett.* **29**, 50-52 (2004).

[44] Z. Lu, C. Schuetz, C. Chen, S. Shi and D. W. Prather, "Micromilled Dielectric PBG Self-Collimation Devices in Millimeter-Wave Regime," *2004 IEEE AP-S International Symposium And USNC /URSI National Radio Science Meeting*, June 20 – June 26, Monterey, California (2004).

[45] J. D. Joannopoulos, R. D. Meade, and J. N. Winn, *Photonic Crystals: Molding the Flow of Light*, Princeton University Press, pp1-76, 1995.

[46] H. Nishihara, M. Haruna, T. Suhara, *Optical Integrated Circuits*, McGraw-Hill Book Company, pp9-21, 1987.

[47] K. M. Ho, C. T. Chan, and C. M. Soukoulis, "Existence of a photonic gap in periodic dielectric structures", *Phys. Rev. Lett.*, **65**, 3152-3155 (1990).

[48] H. Kosaka, T. Kawashima, A. Tomita, M. Notomi, T. Tamamura, T. Sato, and S. Kawakamib, "Self-collimating phenomena in photonic crystals", *Appl. Phys. Letts.* **74**, 1212-1214 (1999).

[49] J. Witzens, M. Loncar, and A. Schere, "Self-collimation in planar photonic crystals", *IEEE Journal of Selected Topics in Quantum Electronics*, **8**, 1246-1257 (2002).

[50] A. Taflove, S. C. Hagness, *Computational Electrodynamics: the Finite-Difference Time-Domain Method*, Artech House, Inc. 2000.

[51] M.L. Dakss, L. Kuhn, P.F. Heidrich, and B.A. Scott, "Grating coupler for efficient excitation of optical guided waves in thin films," *Appl. Phys. Lett.* **16**, 523-525 (1970).

[52] J.-M. Jouanno, D. Zauner, and M. Kristensen, "Low crosstalk planar optical add-drop multiplexer fabricated with UV-induced Bragg gratings," *Electron. Lett.* **33**, 2120–2121 (1997).

[53] T. Tamir and S. Zhang, "Modal transmission-line theory of multilayered grating structures," *J. Lightwave Technol.* **14**, 914–927 (1996).

[54] M. Matsuhara and K. O. Hill, "Optical-waveguide band-rejection filters: Design," *Appl. Opt.* **13**, 2886–2888 (1974).

[55] F. K. Schwering and S. T. Peng, "Design of dielectric grating antennas for millimeter-wave applications," *IEEE Trans. Microwave Theory Tech.* **31**, 199–209 (1983).

[56] H. F. Hammad, Y. M. M. Antar, A. P. Freundorfer, A. Petosa, and M. Sayer, "A Dielectric Gratings Antenna Operating at Ka-Band," *IEEE Antennas and Wireless Propagation Lett.* **1**, 106-108 (2002).

[57] H. F. Hammad, Y. M. M. Antar, A. P. Freundorfer, and M. Sayer "A New Dielectric Grating Antenna at Millimeter-wave Frequency, " *IEEE Trans. On Antennas and Propagation* **52**, 36-44 (2004).

[58] K.L. Klohn, R.E. Horn, H. Jacobs, and E. Freibergs, "Silicon waveguide frequency scanning linear array antenna," *IEEE Trans. Microwave Theory Tech.* **26**, 764-773 (1978).

[59] R.E. Horn, H. Jacobs, E. Freibergs, and K.L. Klohn, "Electronic modulated beam-steerable silicon waveguide array antenna," *IEEE Trans. Microwave Theory Tech.* **28**, 647-653 (1980).

[60] D. W. Prather, S. Shi, D. M. Pustai, C. Chen, S. Venkataraman, A. Sharkawy, G. J. Schneider, and J. A. Murakowski, "Dispersion-based optical routing in photonic crystals," *Opt. Lett.* **29**, 50-52 (2004).

[61] Z. Lu, C. A. Schuetz, S. Shi, C. Chen, G. P. Behrmann, and D. W. Prather, "Experimental demonstration of self-collimation in low-index-contrast photonic crystals in the millimeter-wave regime," *IEEE Trans. Microwave Theory Tech.* **53**, 1362-1368 (2005).

[62] D. M. Pustai, S. Shi, C. Chen, A. Sharkawy, and D. W. Prather, "Analysis of splitters for self-collimated beams in planar photonic crystals," *Opt. Express* **12**, 1823-1831 (2004).

[63] C. Chen, A. Sharkawy, D. M. Pustai, S. Shi, and D. W. Prather, "Optimizing bending efficiency of self-collimated beams in non-channel planar photonic crystal waveguides," *Opt. Express* **11**, 3153-3159 (2003).

[64] R.G. Hunsperger, *Integrated Optics: Theory and Technology*, 3rd edition, pp. 100-103, Springer-Verlag Inc., New York, 1991.

[65] Z. Lu, S. Shi, C. A. Schuetz, and D. W. Prather, "Experimental demonstration of negative refraction imaging in both amplitude and phase," *Opt. Express* **13**, 2007-2012(2005).

[66] Z. Lu, C. Chen, C. A. Schuetz, S. Shi, J. A. Murakowski, G. J. Schneider, and D. W. Prather, "Sub-wavelength imaging by a flat cylindrical lens using optimized negative refraction," *Appl. Phys. Lett.* **87**, 091907 (2005).

[67] Z. Lu, S. Shi, C. A. Schuetz, J. A. Murakowski, and D. W. Prather, "Three-dimensional photonic crystal flat lens by full 3D negative refraction," *Opt. Express* **13**, 5592-5599 (2005).

[68] Z. Lu, C. A. Schuetz, S. Shi, C. Chen, G. P. Behrmann, and D. W. Prather, "Experimental demonstration of self-collimation in low index contrast photonic crystals in the millimeter-wave regime," *IEEE Trans. on Microw. Theory and Techn.* **53**, 1362-1368(2005).

[69] D. W. Prather, S. Shi, S. Venkataraman, Z. Lu, J. Murakowski, G. Schneider, "Self-collimation in 3D photonic crystals," *Proc. of SPIE* **5733**, *Photonic Crystal Materials and Devices III*, Photonic West, San Jose, CA, 2005.

[70] D. W. Prather, S. Venkataraman, S. Shi, G. Schneider, and J. Murakowski, "Design, simulation, and fabrication of 3D self-collimation photonic crystals," *Proceedings of SPIE*, vol. 5595,Active and Passive Optical Components for WDM Communications IV, pp. 45-53, October 2004.

[71] J. Shin and S. Fan, "Conditions for self-collimation in three-dimensional photonic crystals," *Opt. Lett.* **30**, 2397-2399(2005).

[72] R. Iliew, C. Etrich, and F. Lederer, "Self-collimation of light in three-dimensional photonic crystals," *Opt. Express* **13**, 7076-7085 (2005).

[73] S. G. Johnson, and J.D. Joannopoulos, "Block-iterative frequency-dormain methods for Maxwell's equations in a planewave basis," *Opt. Express* **8**, 173-190(2001).

[74] J. Witzens, M. Loncar, and A. Schere, "Self-collimation in planar photonic crystals," *IEEE J. Sel. Topics Quantum Electron.* **8**, 1246–1257(2002).

[75] C.A. Balanis, *Advanced Engineering Electromagnetics*, p. 334, John Wiley & Sons, Inc, 1989.

[76] In our description, the x-axis is along the direction of the penetrated holes and the z-axis is along wave propagation direction.

[77] See, for example, B. A. Saleh and M.C. Teich, *Fundamentals of Photonics*, pp80-107, John Wiley & Sons, Inc., New York, 1991.

[78] P.T. Rakich, *et al*, "Achieving centimeter-scale supercollimation in a large-area two-dimensional photonic crystal," *Nature Materials* **5**, 93-96 (2006).

REPORT DOCUMENTATION PAGE

Form Approved
OMB No. 0704-0188

The public reporting burden for this collection of information is estimated to average 1 hour per response, including the time for reviewing instructions, searching existing data sources, gathering and maintaining the data needed, and completing and reviewing the collection of information. Send comments regarding this burden estimate or any other aspect of this collection of information, including suggestions for reducing the burden, to Department of Defense, Washington Headquarters Services, Directorate for Information Operations and Reports (0704-0188), 1215 Jefferson Davis Highway, Suite 1204, Arlington, VA 22202-4302. Respondents should be aware that notwithstanding any other provision of law, no person shall be subject to any penalty for failing to comply with a collection of information if it does not display a currently valid OMB control number.
PLEASE DO NOT RETURN YOUR FORM TO THE ABOVE ADDRESS.

1. REPORT DATE (DD-MM-YYYY)	2. REPORT TYPE	3. DATES COVERED (From - To)
18-07-2006	Final Technical Report	15 Jan 2005 - 1 Apr 2006

4. TITLE AND SUBTITLE	5a. CONTRACT NUMBER
Dispersion Based Photonic-Crystal Structures for RF Applications	N/A

5b. GRANT NUMBER
N00014-05-1-0161

5c. PROGRAM ELEMENT NUMBER
N/A

6. AUTHOR(S)	5d. PROJECT NUMBER
Dr. Dennis W. Prather	N/A

5e. TASK NUMBER
N/A

5f. WORK UNIT NUMBER
N/A

7. PERFORMING ORGANIZATION NAME(S) AND ADDRESS(ES)	8. PERFORMING ORGANIZATION REPORT NUMBER
University of Delaware - Office of the Vice Provost for Research 210 Hullihen Hall Newark, DE 19716	ELEG332171-063006

9. SPONSORING/MONITORING AGENCY NAME(S) AND ADDRESS(ES)	10. SPONSOR/MONITOR'S ACRONYM(S)
Office of Naval Research Atlanta Regional Office 100 Alabama St. Suite 4R15 Atlanta, GA 30303-3104	
	11. SPONSOR/MONITOR'S REPORT NUMBER(S)

12. DISTRIBUTION/AVAILABILITY STATEMENT
APPROVED FOR PUBLIC RELEASE.

13. SUPPLEMENTARY NOTES

14. ABSTRACT
This work provides a framework for establishing dielectric-based naval communication systems, which are more secure and more efficient, compared to current metallic counterparts. Herein are demonstrated applications of RF PhCs in improving the performance of naval communication systems and decreasing scattering cross-section of naval vessels. Dielectric devices were designed, fabricated, and characterized based on the unique dispersion properties of PhCs to achieve confinement, waveguiding, radiation, and filtering in the microwave to millimeter-wave portion of the electromagnetic spectrum. In particular, dispersion-based guiding, namely self-collimation, in 2D and 3D PhCs was experimentally demonstrated. Self-collimation allows for creating "non-diffractive materials" in which electromagnetic waves can propagate along subwavelength-sized channels without divergence while no specific route is introduced. By combining the self-collimation PhCs, dielectric grating antennas were demon-strated which provide stable performance, compact dimensions, high radiation efficiency, and high coupling efficiency with other dielectric waveguiding devices. We also designed, fabricated, and demonstrated RF channelizers and filters based on the hybrid of properties and lattices of PhCs.

15. SUBJECT TERMS

Photonic crystal, dispersion, dielectric device, self-collimation, millimeter-wave, dielectric grating antennas, filter, channelizer, naval communication

16. SECURITY CLASSIFICATION OF:			17. LIMITATION OF ABSTRACT	18. NUMBER OF PAGES	19a. NAME OF RESPONSIBLE PERSON
a. REPORT	b. ABSTRACT	c. THIS PAGE	UU	39	Dr. Dennis W. Prather
U	U	U			19b. TELEPHONE NUMBER (Include area code) (302) 831-8170

Standard Form 298 (Rev. 8/98)
Prescribed by ANSI Std. Z39.18